สัญญาเลขที่ R2557B091

รายงานวิจัยฉบับสมบูรณ์

การเตรียมและการหาลักษณะเฉพาะของเซรามิก (1-x-y)$Bi_{0.5}Na_{0.5}TiO_3$-x$Bi_{0.5}K_{0.5}TiO_3$–y$BiFeO_3$ ที่เตรียมด้วยวิธีการเผาไหม้

Fabrication and Characterization of (1-x-y)$Bi_{0.5}Na_{0.5}TiO_3$-x$Bi_{0.5}K_{0.5}TiO_3$-y$BiFeO_3$ Ceramics Prepared via Combustion Technique

ผศ. ดร. ธีระชัย บงการณ์
ภาควิชาฟิสิกส์ คณะวิทยาศาสตร์ มหาวิทยาลัยนเรศวร

งานวิจัยนี้ได้รับการสนับสนุนงบประมาณจาก
งบประมาณแผ่นดิน มหาวิทยาลัยนเรศวร ประจำปีงบประมาณ 2557

กิตติกรรมประกาศ

งานวิจัยนี้ได้รับกาสนับสนุนงบประมาณจาก งบประมาณแผ่นดิน มหาวิทยาลัยนเรศวร ประจำปีงบประมาณ 2557 ผู้วิจัยขอขอบพระคุณ ณ โอกาสนี้

ขอขอบคุณเจ้าหน้าที่ภาควิชาฟิสิกส์ คณะวิทยาศาสตร์ มหาวิทยาลัยนเรศวร ทุกท่านซึ่งอำนวยความสะดวกเกี่ยวกับอุปกรณ์เครื่องมือต่างๆ

ขอขอบคุณ Science Lab Center คณะวิทยาศาสตร์ มหาวิทยาลัยนเรศวร ที่สนับสนุนเครื่องมือและอุปกรณ์ในการทำวิจัย

ผศ.ดร.ธีระชัย บงการณ์ และคณะ

Research Topic: Fabrication and Characterization of (1-x-y)$Bi_{0.5}Na_{0.5}TiO_3$-x$Bi_{0.5}K_{0.5}TiO_3$-yBiFeO $_3$ Ceramics Prepared via Combustion Technique

Researcher: Assist. Prof. Dr.Theerachai Bongkarn

ABSTRACT

(1-*x*-*y*)$Bi_{0.5}Na_{0.5}TiO_3$ –*x*$Bi_{0.5}K_{0.5}TiO_3$ –*y*$BiFeO_3$ (abbreviated as BNKFT-*x*/*y* with $0.12 \leq x \leq 0.24$, $0 \leq y \leq 0.07$) lead-free piezoelectric ceramics have been prepared by combustion technique. The effect of amounts of *x* and *y* on structures and electrical properties were examined. The powders and ceramics can be well calcined and sintered at 750 ^{o}C for 2 h and 1025 ^{o}C-1050 ^{o}C, respectively. The results indicated that the crystalline structure and microstructure change with the increase of *x* and *y* concentrations. XRD results of BNKFT-*x*/0.03 and BNKFT-0.18/*y* ceramics with $0.12 \leq x \leq 0.24$ and $0 \leq y \leq 0.07$ showed the rhombohedral-teragonal morphotropic phase boundary (MPB). The addition of *y* caused a promoted grain growth while the addition of *x* suppressed the grain growth. The highest densities (ρ = 5.85 g cm^{-3}), superior dielectric properties at T_c (ε_r = 7,846 and tanδ = 0.02), remnant polarization measured at 40 kV/cm (20.1μC/cm^2) and piezoelectric coefficient (d_{33} = 213 pC/N) were obtained where x = 0.18 and y = 0.03.

CHAPTER 1

INTRODUCTION

1.1 Overview

As well known, piezoelectric materials have wide applications in electronic and microelectric devices. The most widely used piezoelectric materials are $PbZrO_3$-$PbTiO_3$ (PZT) based ceramics. However, in the process of obtaining this material, it is necessary to maintain the atmosphere enriched with the vapor of lead oxide (PbO), which is opposite to the needs of environmental protection because of the toxicity. Furthermore, many countries have restricted to using lead oxide by drafting legislation. So, it is necessary and urgent to search for lead-free piezoelectric ceramics with excellent piezoelectric properties [1].

$Bi_{0.5}Na_{0.5}TiO_3$ (abbreviate to BNT), discovered by Smolenskii et al. in 1960 [1,2], is an ABO_3 type ferroelectric with perovskite phase. BNT is considered to be a promising candidate of lead-free piezoelectric ceramics with a relatively large remnant polarization (P_r = 38 $\mu C/cm^2$) and a high Curie temperature (T_c = 320 °C) [3,4]. However, the pure BNT ceramics has a high coercive field (E_c=7.3 kV/mm), making the poling of the ceramics extremely difficult. In addition, pure BNT ceramic usually exhibits very poor piezoelectricity (d_{33}=58 pC/N). To decrease the coercive field and improve the piezoelectric properties, a number of solid solutions of BNT with ABO_3-type ferroelectrics or non-ferroelectrics, such as BNT-$BaTiO_3$ [5], BNT-$NaNbO_3$ [6], BNT-$CaTiO_3$ [7], BNT-$SrTiO_3$ [7], BNT-$Bi_{0.5}K_{0.5}TiO_3$ [1] have been studied extensively. Xinyou *et al.* [5] reported that the dielectric constant (ε_r), the loss tangent ($\tan\delta$) and the piezoelectric constant (d_{33}) of 0.94 BNT-0.06$BaTiO_3$ ceramics are 1650, 0.048 and 120 pC/N. In case of 0.98BNT-0.02$CaTiO_3$, 0.80BNT-0.20$SrTiO_3$ and 0.98BNT-0.02$NaNbO_3$, the d_{33} values were 75 [7], 133 [7] and 88 pC/N [6]. 0.82BNT-0.18$Bi_{0.5}K_{0.5}TiO_3$ (BNT-BKT) ceramics demonstrated the ε_r, $\tan\delta$, d_{33}, k_p

and E_c of 893, 0.037, 144 pC/N, 29.0 % and 4 kV/mm [1]. Among these compositions, BNT-BKT ceramics have exhibited excellent piezoelectric properties, but still far from satisfaction in terms of practical application.

The ternary system has been demonstrated that favorable design can improve piezoelectric and ferroelectric properties [8-19]. The ternary system of BNT-BKT with $BaTiO_3$ (BT) [10-12], $LiNbO_3$ [13], $(K_{0.5}Na_{0.5})NbO_3$ (KNN) [14], $(Bi_{0.5}Li_{0.5})TiO_3$ (BLT) [15,16], and $BiFeO_3$ (BF) [17-19] were intensively investigated. Among the solid solutions that have been developed so far, $(1\text{-}x\text{-}y)Bi_{0.5}Na_{0.5}TiO_3\text{–}xBi_{0.5}K_{0.5}TiO_3\text{–}yBiFeO_3$ (BNKFT) system has attracted considerable attentions. Zhou *et al.* [18] reported that the optimum values of d_{33} and k_p are 170 pC/N and 36.6 % obtained from $0.79Bi_{0.5}Na_{0.5}TiO_3$-$0.18Bi_{0.5}K_{0.5}TiO_3$-$0.03BiFeO_3$ ceramics.

BNKFT has been prepared by solid state reaction method, consisting of a calcination stage above 900 °C and sintering stage above 1150 °C for 3-5 h [18]. Although solid-state reaction method is relatively simple but it is time consuming, energy intensive and poor quality ceramic is obtained. Recently, our previous works have successfully fabricated high quality different oxides ceramics such as: $(Ba_{1-x}Sr_x)(Zr_xTi_{1-x})O_3$ [20], $Ba(Ti_{1-x}Zr_x)O_3$ [21], $(Pb_{1-x}Ba_xTiO_3)$ [22], $BaZrO_3$[23] by the combustion technique. The advantages of this technique include inexpensive precursors, simple preparation process, and resulting good electrical properties with lower firing temperature and shorter dwell time [24-26]. Furthermore, from a survey of the literature, BNKFT ceramics, prepared by the combustion method, have not been studied. Thus, in this work, $(1\text{-}x\text{-}y)Bi_{0.5}Na_{0.5}TiO_3\text{–}xBi_{0.5}K_{0.5}TiO_3\text{–}yBiFeO_3$ (x=0.12-0.24, y=0-0.07) ceramics were prepared by the combustion method. The effects of firing temperatures and the change of the x and y content on the phase formation, microstructure, and electrical properties of ceramics were investigated.

1.2 Objectives of this work

The objectives of this research are as follow:

1. To prepare BNKFT ceramics ternary system using combustion technique.
2. To investigated the optimum calcination and sintering conditions of BNKFT ceramics for combustion preparation.
3. To study the effect of calcination and sintering temperatures on the crystal structure, microstructure, dielectric properties and piezoelectric properties of BNKFT ceramics prepared via the combustion technique.
4. To study the effect of $BiFeO_3$ co-doped on the properties of $Bi_{0.5}Na_{0.5}TiO_3$–$Bi_{0.5}K_{0.5}TiO_3$ based ceramics and special significance was focused on seeking the MPB composition.

CHAPTER 2

THEORY AND LITERATURE

2.1 Basic Definition

2.1.1 Perovskite Structure

Since the ferroelectric properties of barium titanate were reported by von Hippel in 1945 and others, ABO_3 compound with the perovskite structure have been studied extensively [27,28]. These studies have resulted in the discovery of many new ferroelectric and piezoelectric materials. Most of the literatures on perovskite-type compound have been concentrated on these properties.

Perovskite is the name of the mineral calcium titanate ($CaTiO_3$). Most of the useful piezoelectric (ferroelectric) ceramics, such as barium titanate ($BaTiO_3$), lead titanate ($PbTiO_3$), lead zirconate titanate ($PbZr_{1-x}Ti_xO_3$), lead lanthanum zirconate titanate (PLZT), potassium niobate ($KNbO_3$), potassium sodium niobate ($KNa_xNb_{1-x}O_3$), have perovskite structure. These oxide ceramics have the general chemical formular ABO_3, where O is oxygen in the centers of the faces, A represents a cation with a larger ionic radius on the corners, and Ba cation with a smaller ionic radious in the body center [29-31]. Figure 2.1 shows a cubic ABO_3 perovskite-type unit cell and three–dimensional network of BO_6-octrahedral.

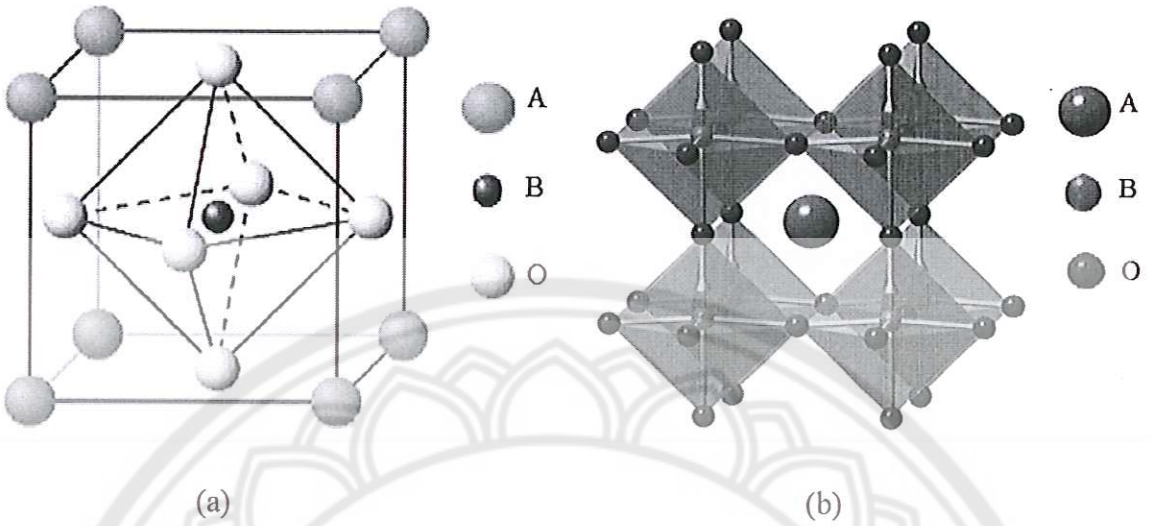

(a) (b)

Figure 2.1 The perovskite structure as (a) an ABO_3 perovskite-type unit cell and (b) three-dimensional network of BO_6 octahedral.

A perovskite structure is essentially a three-dimensional network of BO_6 octrahedral as shown in Figure 2.1(b). In Figure 2.1(a), A sites are occupied by Ba^{2+}, Pb^{2+}, K^+ or Na^+ ions, and B sites by Ti^{4+}, Zr^{4+}, Nb^{5+} or Ta^{5+} ions.

2.1.2 Piezoelectricity

Piezoelectricity was discovered in 1880 by Jacques and Pierre Curie during their systematic study of the effect of pressure on the generation of electrical charge by crystals such as quartz, zincblend, and tourmaline [29-30,32]. The name "piezo" is derived from the Greek, meaning "to press", hence piezoelectricity is the generation of electricity as a result of mechanical pressure. Many piezoelectric materials are not ferroelectric but all ferroelectrics are piezoelectric. Two effects are operative in piezoelectricity. The direct effect is identified with the phenomenon whereby electrical charge (polarization) is generated from a mechanical stress, whereas the converse effect is associated with the mechanical movement generated by the application of an electrical field. Both of these effects are illustrated in Figure 2.2

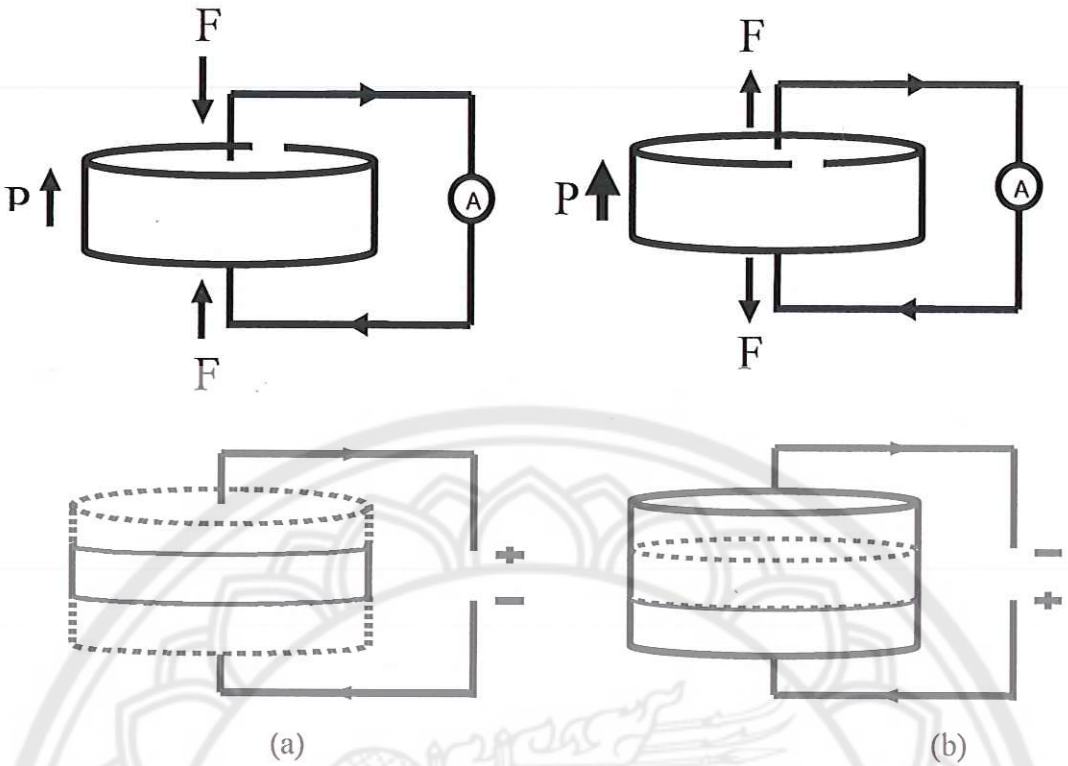

Figure 2.2 Piezoelectric effects in ferroelectric ceramics (a) direct effect (b) converse effect [29].

The basic equations that describe these two effects in regard to electric and elastic properties are

$$D = dT + \varepsilon^T E \tag{2.1}$$

$$S = s^E T + dE \tag{2.2}$$

Where D is the dielectric displacement (consider it equal to polarization), T the stress, E the electric field, S the strain, d a piezoelectric coefficient, s the material compliance (inverse of modulus of elasticity), and ε the dielectric constant (permittivity). The subscripts indicate a quantity held constant: in the case of ε^T, the stress is held constant, which means that the piezoelectric element is mechanically unconstrained, and, in the case of s^E, the electric field is held constant, which means the electrodes on the element are shorted together.

2.1.3 Ferroelectrics

Ferroelectricity is a phenomenon which was discovered by Valasek in 1921 [33]. It has become customary to call ferroelectricity the phenomenon exhibited by these crystals and ferroelectric the crystal by themselves. This is due to a formal similarity of the ferroelectric phenomenon with that of ferromagnetism. The similarity is mainly phenomenological. As ferromagnetic materials exhibit a spontaneous magnetization and hysteresis effects in the relationship between magnetization and magnetic field, ferroelectric crystals show a spontaneous electric polarization and hysteresis effects in the relation between dielectric displacement and electric field. This behavior is mostly observed in certain temperature regions below by transition temperature (Curie temperature) where those above are no longer ferroelectric.

The crystal symmetries of the paraelectric and ferroelectric phase are important factor in displaying the ferroelectric behavior of the materials. The lattice structure described by the Bravais unit cell of the crystal governs the crystal symmetry. Though there are thousands of crystals in nature, they all can be grouped together into 230 microscopic symmetry types or space group based on systemetry elements. It can be shown by the inspection of the 230 space groups that there are just 32 point groups. As shown in Figure 2.3, the 32 point groups can be further classified into (a) crystal having a center of symmetry and (b) crystals which do not possess a center of symmetry (noncentrosymmetric). There are 21 classes of noncentrosymmetric, a necessary condition for piezoelectricity to exist, and only 20 are piezoelectric. Among these 20 point groups, only 10 can display a spontaneous polarization, which is designated as pyroelectric. A subgroup of the spontaneous polarized pyroelectric is a category of materials known as ferroelectrics. Ferroelectrics are a special class of materials in which a permanent electric dipole can be reoriented between equilibrium states by the external electric field

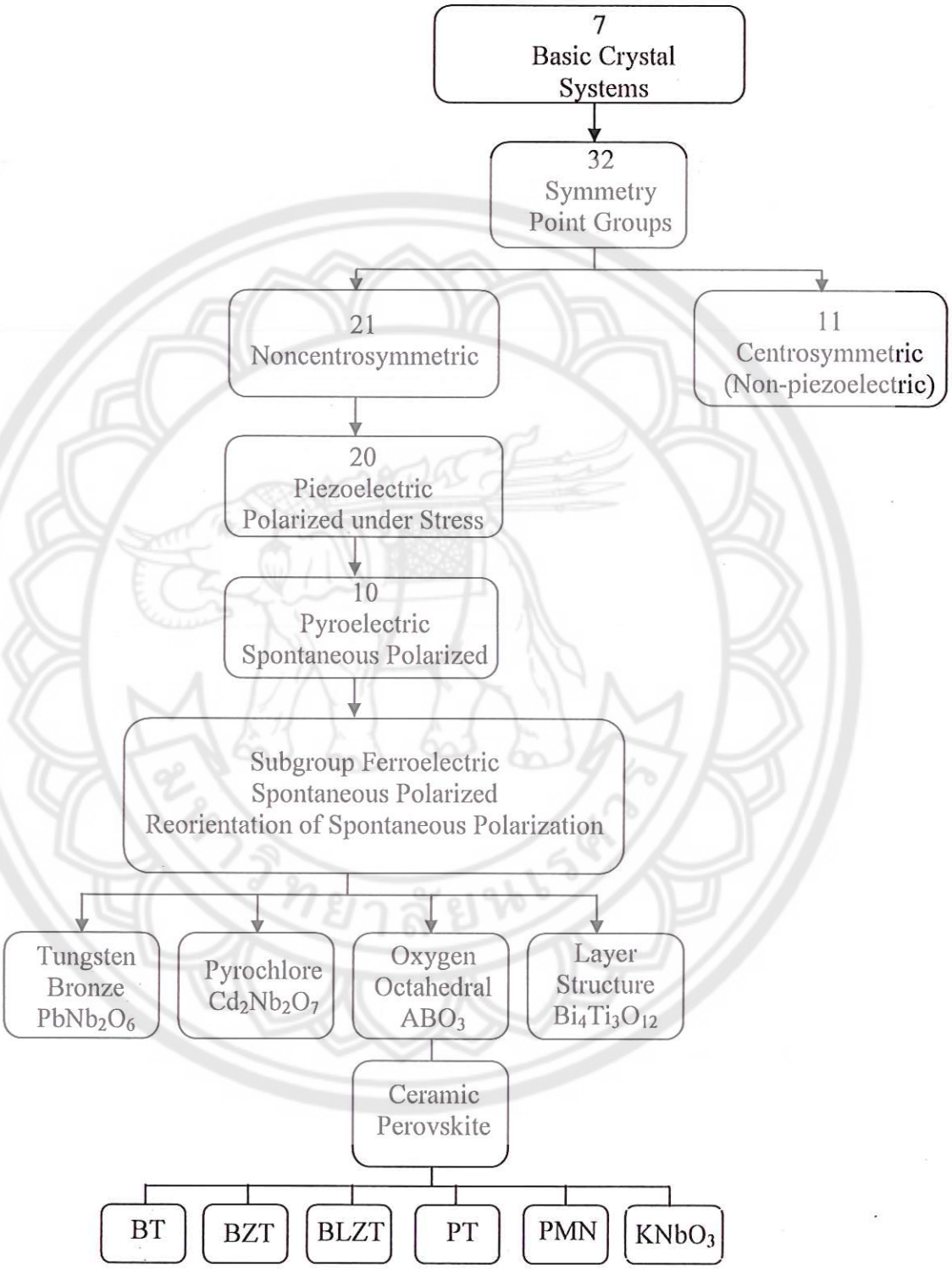

Figure 2.3 Interrelationship of piezoelectric and subgroups on the basis of symmetry [29].

Continuing Valasek's analogy between ferroelectric and ferromagnetic, the dependence of the polarization on applied electric field can be seen by polarization versus electric field i.e. (P-E) hysteresis loop as shown in Figure 2.4. The hysteresis loop is typically observed using the simple circuit described by Sawyer-Tower [34]. One parameters obtained from the hysteresis loop measurement, the remnant polarization (P_r) is the crystal spontaneous polarizes along one of the allowed direction without applied electric field. The field required to reverse the polarization is known as the coercive field (E_c).

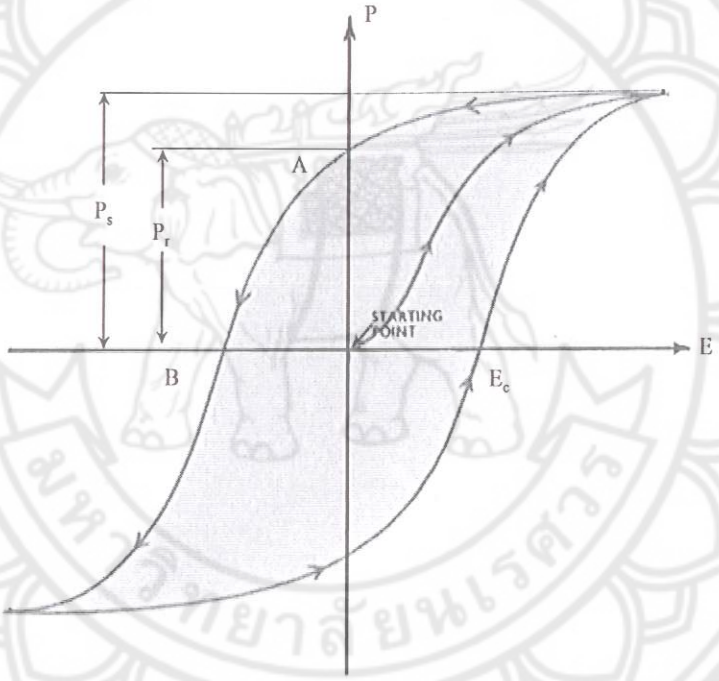

Figure 2.4 A ferroelectric hysteresis loop [35].

2.1.3.1 Normal ferroelectric

Normal ferroelectric materials have a sharp phase transition which occurs at a specific temperature called the Curie temperature, T_c. The T_c is the temperature which the crystal

structure transforms from the paraelectric state into the ferroelectric state as vice versa [36-38]. In the paraelectric state, the dielectric permittivity obeys the Curie-Weiss law:

$$\varepsilon_r = \frac{C}{T - T_0} \tag{2.3}$$

Where C is the Curie-Weiss constant, T is the temperature and, T_0 is the Curie-Weiss temperature. The Curie temperature (T_c) and the Curie-Weiss temperature (T_0, Θ) should not be confused. The Curie temperature is the actual transformation temperature, but the Curie-Weiss temperature is found by the extrapolating the plot of the Curie-Weiss law, as shown in Figure 2.5. The Curie temperature and Curie-Weiss temperature typically differ by only a small amount that depends on the type of phase formation the material undergoes. The Curie-Weiss temperature can be as much as ten degrees lower than the Curie temperature for first-order phase transformations and the two can be nearly equal for second-order phase transformations (first order phase transformations are those in which the first derivative of the free energy, with respect to temperature, is discontinuous; second order phase transitions are those in which the second derivative is discontinuous).

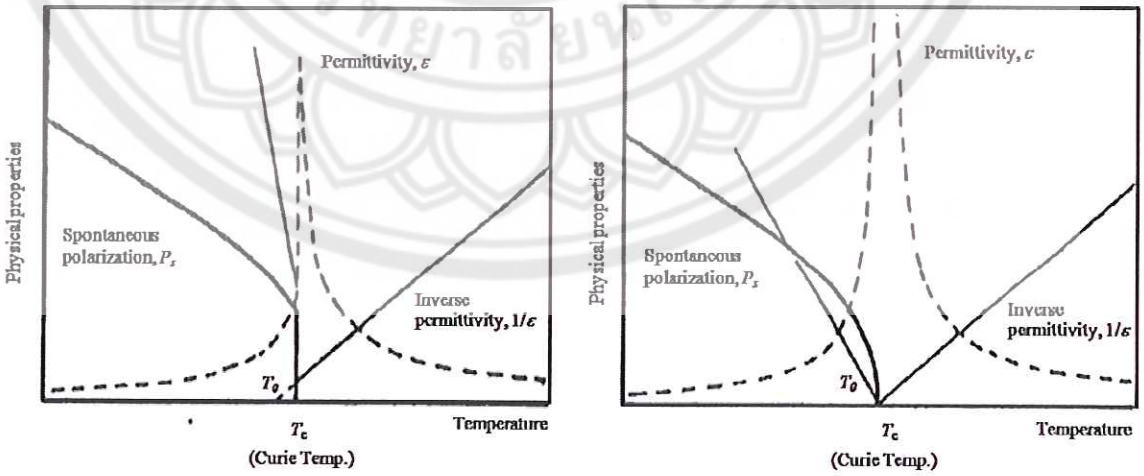

(a) (b)

Figure 2.5 Phase transition in a ferroelectric (a) first order and (b) second order [39].

2.1.3.2 Relaxor ferroelectric

The relaxor behaviors, recognized by Cross [40], of the ferroelectric materials are divided into two main categories as normal and relaxor ferroelectrics. Several material properties distinguish normal and relaxor ferroelectrics are summarized in Table 2.1 and below:

(i) The sharp well-defined phase transition temperature (Curie temperature) found for normal ferroelectrics is absent for relaxors. The dielectric constant maximum does not distinguish the exact paraelectric to ferroelectric phase transition as in normal ferroelectrics. The paraelectric to ferroelectric phase transition becomes broad and diffuse in relaxor and Curie ranges replace the Curie temperature. The permittivity of relaxor is also dispersive in nature at radio frequencies, which the permittivity decreases and the temperature of the dielectric constant maximum (T_m) shifts to higher temperature with increasing frequency. The example of broad dielectric and diffuse phase transition.

(ii) In relaxor ferroelectric, the dielectric constant does not follow Curie-Weiss law behavior above the ferroelectric transition. Instead, relaxers follow Curie-Weiss square law (sometimes called the quadratic Curie-Weiss law):

$$\frac{1}{\varepsilon_r} - \frac{1}{\varepsilon_m} = \frac{(T-T_m)^2}{C'} \tag{2.4}$$

where ε_r is the relative dielectric constant, ε_m is the dielectric constant maximum, T_c is the temperature of the dielectric constant maximum and C' is the modified Curie-Weiss constant. This quadratic relation is valid for materials that display diffuse phase transitions. Most materials; however, show intermediate behavior between the linear and quadratic limits.

Uchino *et al.* proposed a variation power law as the modified Curie-Weiss law [41]

$$\frac{1}{\varepsilon_r} - \frac{1}{\varepsilon_m} = \frac{(T - T_m)^{\gamma}}{C'} \tag{2.5}$$

where γ is the critical exponent. The value of the critical exponent can vary from $\gamma = 1$, for purely normal ferroelectric, to $\gamma = 2$, for purely relaxor ferroelectrics. The qualitative method to determine the parameter of relaxor ferroelectric is by plotting the inverse dielectric constant as a function of temperature as a log-log scale.

(iii) Another feature which distinguishes normal and relaxor ferroelectrics is the behavior of polarization. The relatively rapid decrease of the polarization to zero is found in normal ferroelectrics at T_c. This gradual decrease extends to temperature above T_m before reaching zero. This can be observed in P-E hysteresis loops. At temperature well below T_m, relaxors show typical P-E hysteresis loop; however, the loops decay slowly into simple non-linearity as the temperature increases through the Curie range.

(iv) As temperature decreases, the number of polar regions increases so that the regions are in contact; however, since these regions are oriented along different polarization directions the crystal still appears isotropic. Several characteristics are caused by the polar regions orienting along difference axes. First, relaxor ferroelectrics exhibit weak remnant polarization. Second, due to the long coherence length of XRD, relaxor ferroelectrics appear cubic since they do not exhibit x-ray peak splitting. Third, under optical microscopy, relaxor ferroelectrics exhibit negligible birefringence.

Table 2.1 Different properties of normal and relaxor ferroelectrics [42].

Properties	**normal ferroelectrics**	**relaxor ferroelectrics**
Permittivity temperature dependence $\varepsilon_r = \varepsilon_r(T)$	Sharp 1st or 2nd order phase transition at Curie temperature (T_c)	Broad-diffuse phase transition around Curie maxima (T_m)
Permittivity temperature and frequency dependence $\varepsilon_r = \varepsilon_r(T, \omega)$	Weak frequency dependence	Strong frequency dependence
Permittivity behavior in paraelectric range ($>T_c$)	Follow Curie-Weiss law $\varepsilon_r = C/(T = T_0)$	Follow Curie-Weiss square law $1/\varepsilon_r = 1/\varepsilon_m + (T-T_m)^2 / 2\varepsilon_m\delta^2$
Remnant polarization	Strong remnant polarization	Weak remnant polarization
Scattering of light	Strong anisotropy (birefringent)	Very weak anisotropy to light (pseudo-cubic)
Diffraction of X-ray	Line splitting owing to spontaneous deformation from paraelectric to ferroelectric phase	No X-ray line slitting giving a pseudo-cubic structure

2.1.4 Antiferroelectric

An antiferroelectric crystal is defined as a crystal whose structure can be considered as being composed of two sublattices polarized spontaneously in antiparallel directions and in which a ferroelectric phase can be induced by applying an electric field. Experimentally, the reversal of the spontaneous polarization in ferroelectrics is observed as a single hysteresis loop, and the induced phase transition in antiferroelectrics as a double hysteresis loop (Figure 2.6), when a low-frequency ac field of a suitable strength is applied [43].

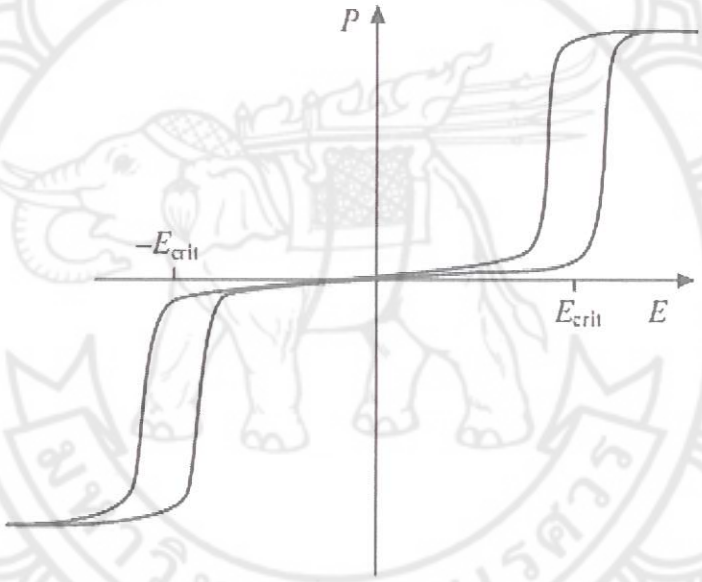

Figure 2.6 Antiferroelectric hysteresis loop [43].

2.1.5 Paraelectric

Paraelectricity is the ability of many materials (specifically ceramic crystals) to become polarized under an applied electric field. Unlike Ferroelectricity; this can happen even if there is no permanent electric dipole that exists in the material, and removal of the fields results in the polarization in the material returning to zero, as shown in Figure 2.7. The mechanisms which give rise to paraelectric behavior are the distortion of individual ions

(displacement of the electron cloud from the nucleus) and the polarization of molecules or combinations of ions or defects. Paraelectricity occurs in crystal phases in which electric dipoles are unaligned (i.e. unordered domains that are electrically charged) and thus have the potential to align in an external electric field and strengthen it. In comparison to the ferroelectric phase, the domains are unordered and the internal field is weak. The $LiNbO_3$ crystal is ferroelectric below 1430 K, and above this temperature it turns to paraelectric phase. Other perovskites similarly exhibit paraelectricity at high temperatures [44].

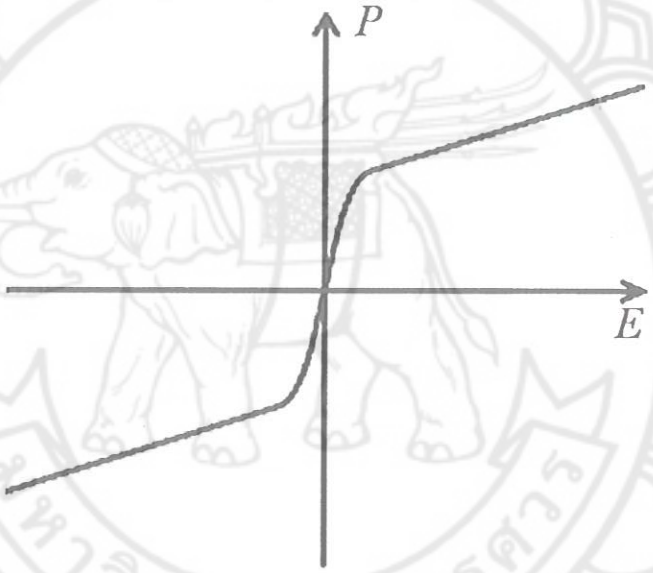

Figure 2.7 Paraelectric hysteresis loop [44].

2.1.6 Combustion technique

Combustion technique has emerged as an important technique for the synthesis and processing of advanced ceramics. The advantages of this technique include inexpensive precursors, simple preparation process, and resulting good electrical properties with lower firing temperature and shorter dwell time [24]. Some other advantages of combustion technique are: (i) Use of relatively simple equipment (ii) Formation of high-purity products

(iii) Stabilization of metastable phases and (iv) Formation of virtually any size and shape products. The features of the combustion methods compare with other methods is listed in Table 2.2.

Solid filme phenomenon (the combustion process, in which starting reactants and combustion product are in the solid state) was discovered in 1967. It was developed on basis of the method of self-propagating high temperature synthesis (SHS). SHS represents a self-adjusting process, in which the product formation generally is both a cause and a consequence of combustion. Figure 2.8 shows wave complex in SHS processes generally has a complex structure [25].

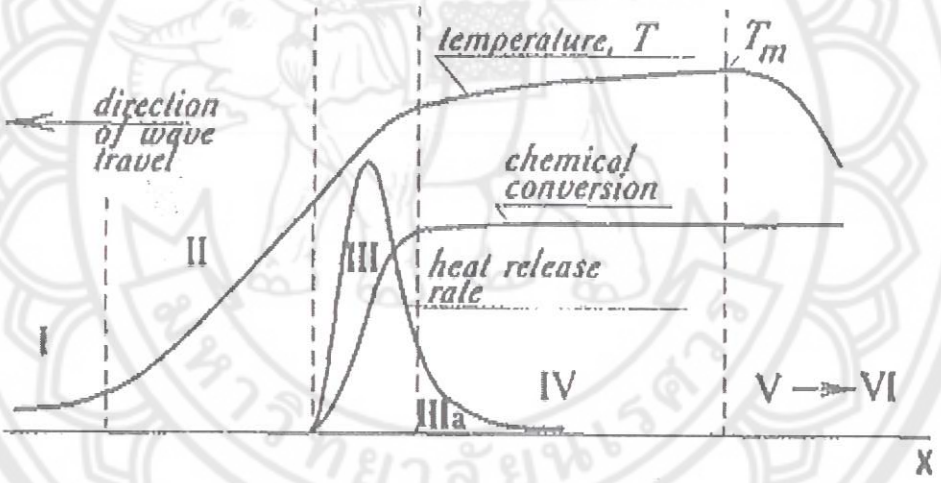

Figure 2.8 Wave complexes in SHS systems. Spatial coordinate in the steady combustion wave: I starting reactants; II preflame; III zone of main heat release; IIIa zone of afterburning; IV phase and structure formation in primary products; V cooling of products; VI final SHS products [25].

In modern concepts of the combustion theory and structure mackrokinetics of chemical reactions, the combustion front the separates the preflame zone and the zone of chemical conversion is an important element of this structure. The heat release that influences the front propagation occurs in the zone of chemical conversion, which is adjacent to the

combustion front. In the preflame zone, the intense heat transfer takes place, but the chemical reactions are not still occurring. The leading edge of the zone of chemical conversion (heat release) is important in SHS and the extent of chemical conversion in this stage may be appreciable. After the completion of chemical reactions, the phase and structure transformations in the primary combustion products continue to occur. These processes determine the structure of final products and play on an important role in forming the properties of the materials synthesized. In zone V and VI are cooling of products and final SHS process. These may also influence on structure ordering in final products. If a product cools down slowly, self-annealing will take place, and the product will acquire the equilibrium structure. Conversely, if the cooling rate is high, quenching will occur and the product will remain non equilibrium (crystal lattice has no time to be formed). Therefore, the rate of SHS processes is determined by the patterns of heat release and transfer in the main combustion zones, whereas the characteristics of final products depend on the post processes (phase and structure formation, conditions and rate of cooling).

Table 2.2 Features of some methods for producing high quality powders and the characteristics of the powders [24].

Method	Furnace Synthesis	Co-precipitation from solutions	Hydrothermal synthesis	Synthesis in the gas phase	Carbothermal reduction	Combustion methods
Characteristics of the powder	Low	High	High	Medium to low	Medium to low	Medium to high
Purity	Not	Yes	Yes	Yes	Yes-not	Yes
Small grain particle size	No	Good	Good	Medium	Medium	Medium
Compositional control	Yes	Not	Not	Not	Not	Yes
Features of the method	Yes	Not	Not	Not	Yes	Not-yes
Low cost of installations						
Consumption of external energy	High	High	High	Medium	Medium	Low
sources						
Short time of synthesis	Not	Not	Not	Yes	Not	Yes
Simplicity and low number of main	Yes	Not	Not	Not	Not	Yes
processing steps						
Main applications	Powders of low quality	Powders of simple and complex oxides	Powders of simple and complex oxides	Powders of simple covalent compounds	Powders of simple covalent compounds	Powder of covalent and intermetallic compounds

2.2 One Component Systems

Useful lead-free materials are often binary or ternary solid solutions. Before discussing these more complex material systems in Sections 2.3 and 2.4, this section introduces and discusses the member compositions of based ceramics.

2.2.1 $(Bi_{0.5}Na_{0.5})TiO_3$ (BNT)

Since BNT was discovered by Smolenskii *et al.* in 1960 [2,45], it has gained a lot of attentions from various aspects. It has high Curie temperature (T_c=320 °C). Recently, detailed studies on the structure transformation of BNT single crystals have been carries out by Hiruma *et al.* using x-ray diffraction. They found that the pure BNT is a perovskite-structured ferroelectric with rhombohedral symmetry at room temperature (RT), and its phase transitions are complicated [46]. The phase transition temperatures T_{R-T} from rhombohedral to tetragonal and T_{T-C} from tetragonal to cubic are approximately 230 and 320°c upon heating, respectively, for BNT single crystals. Lee *et al.* [47] studies the lattice parameter of BNT ceramic system calculated by the Rietveld method with XRD patterns, and they reported that the lattice constants of BNT ceramics are a=3.888 Å.

Lencka *et al.* [48] studied the microstructure of BNT powder prepared by hydrothermal method, were investigated using field emission scanning microscopy (FESEM), x-ray diffraction (XRD) and specific surface areas were measured by multipoint BET technique. The average particle size calculated from FESEM range from 40 and 150 nm can be seen in Figure 2.9. Crystallite sizes calculated from the XRD peak broadening range from 13 to 28 nm. The measured specific surface areas range from 20.0 m^2/g to 27.6 m^2/g. Saradhi *et al.* [49] investigated the grain size of BNT ceramics were prepared by conventional double sintering method and analyzed by scanning electron microscope (SEM). They revealed that the average grain size ranged from 1 to 3 μm, corresponding to the result of Zuo *et al.* [50].

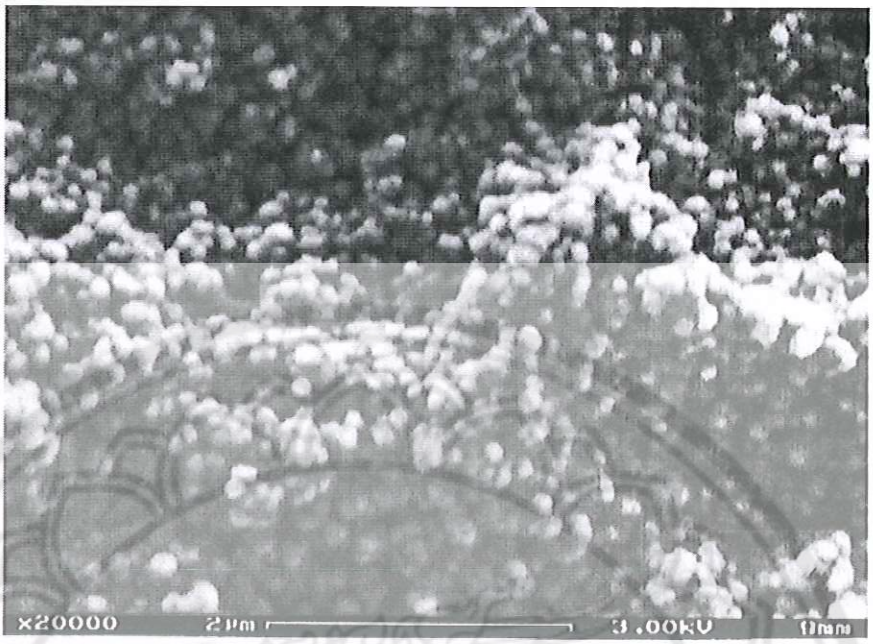

Figure 2.9 FESEM micrograph of the BNT powders [48].

The temperature dependences of the dielectric constant (ε_s) and the loss tangent (tanδ) from 20 Hz to 1 MHz of BNT ceramics between RT and 500 °C are shown in Figure 2.10. There are two dielectric anomalies peaks. The appearance of first temperature peak (T_d) is caused by the phase transition from rhombohedral ferroelectric to tetragonal anti-ferroelectric phase. The appearance of second temperature peak (T_m) can be explained by the transition from tetragonal anti-ferroelectric to cubic paraelectric phase. T_d and T_m occurred in a temperature at 187 °C and 325 °C. The tan δ curves of the BNT reveal only one peak near the temperature of T_d and tan δ sharply increases when temperature is higher than T_m [46].

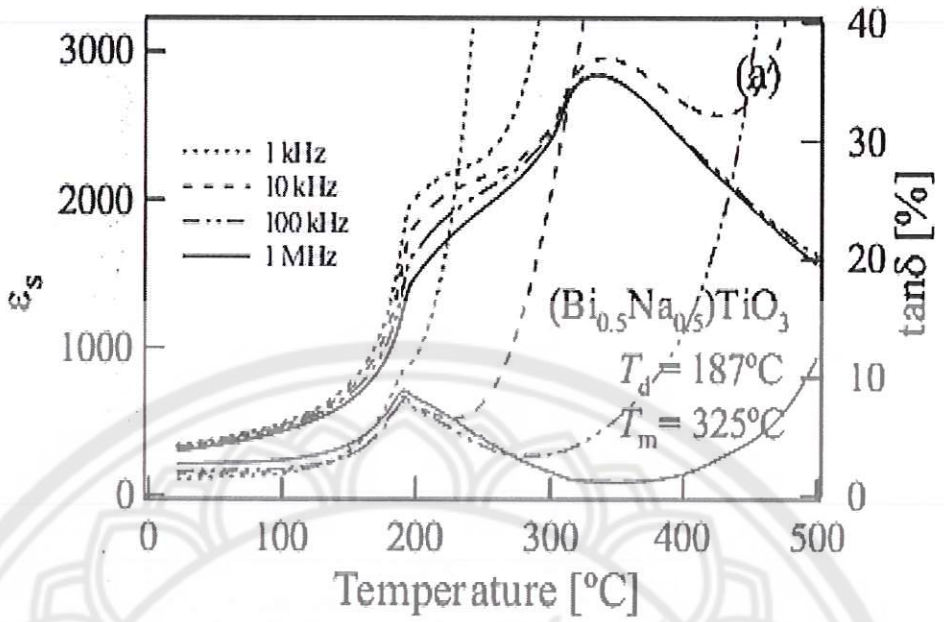

Figure 2.10 Temperature dependences of dielectric constant (ε_r) and loss tangent (tanδ) in temperature range from RT to 500 C of BNT ceramics [46].

The BNT ceramics shows the strong ferroelectric property of a large remnant polarization and relatively high piezoelectric properties compared with other lead-free piezoelectric ceramics. Zuo *et al.* [50] reported that the remnant polarizations, piezoelectric constant and coupling factor of BNT are 38 $\mu C/cm^2$, 75 pC/N and 15.4 %. Nevertheless, the applications of BNT are limited by its high coercive field and its high conductivity. Coercive fields vary greatly between 2 kV/mm for sol-gel derived BNT and 7.3 kV/mm for BNT prepared by a mixed oxide route [51]. To solve these problems and improve the electric properties, various types of compounds were added into BNT to form solid solution, such as $BaTiO_3$, $SrTiO_3$, $CaTiO_3$, $Bi_{0.5}K_{0.5}TiO_3$, $NaNbO_3$, $Ba(Cu_{0.5}W_{0.5})O_3$, and discussing complex material in section 2.3.

2.2.2 $(Bi_{0.5}K_{0.5})TiO_3$ (BKT)

BKT was first determined to be ferroelectric by Smolenskii *et al* [52]. in 1961 at the same time as BNT. Its unit cell is similar is that if BNT but with all the sodium ions replaced by potassium ions. It is a tetragonal ferroelectric perovskite at room temperature and a relatively high curie temperature T_c of 380 °C. Above the Curie temperature BKT is cubic paraelectric [53]. Ivanova *et al.* [54], reported the lattice parameter of BKT as a = 0.3913 nm, c = 0.3990 nm at room temperature.

SEM micrograph of BKT powder was studied by Hou *et al.* [55], and they reported that the particles size very small and relatively uniform, can be seen in Figure 2.11. The average particle size was between 100 and 200 nm. FESEM micrograph of the BKT powders demonstrated a uniform spherical particle with the diameter ranges from 40 to 150 nm, which was studies by Lencka *et al* [48], as shown in Figure 2.12.

The dielectric constant (ε_r) and dielectric loss (tanδ) of BKT ceramics were studied by Hiruma et al [56]. The ε_r and tanδ at room temperature of BKT are 524 and 6.8% at 1MHz. Some authors showed the values of room temperature dielectric constant ε_r and loss tan δ at 1 kHz are 733 and 4.8 %. Yang *et al.* [57] studies the dielectric relaxer properties of ferroelectric BKT single crystal by molten salt method. They reported that the maximum in ε_r is diffusive and centered at around 357 °C accompanied by a strong dispersion of dielectric maximum temperature (T_m) with frequency. Upon increasing the field frequency, the dielectric maximum decreases, while the Curie temperature increases (from 337 C at 1 kHz to 362 at 1000 kHz), showing the relaxer behavior of the present ceramics, as shown in Figure 2.13.

The polarization hysteresis behavior of BKT measured at several temperatures was also reported, as shown in Figure 2.14. Hysteresis loop is observed even at temperatures as high as 260 °C [56]. As expected, the coercive field also gradually decreases with an

increase in temperature, as does the remnant polarization. The remnant polarization (P_r = 22.2 μC/cm^2) and 52.5 kV/cm^2 of BKT were reported [58].

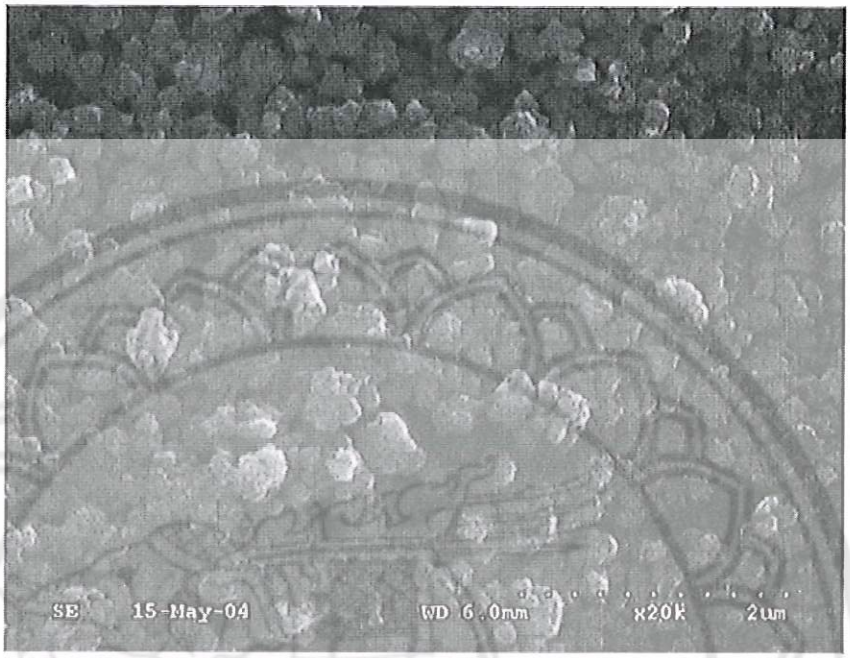

Figure 2.11 FESEM micrograph of the BKT powders was studied by Hou *et al.* [55].

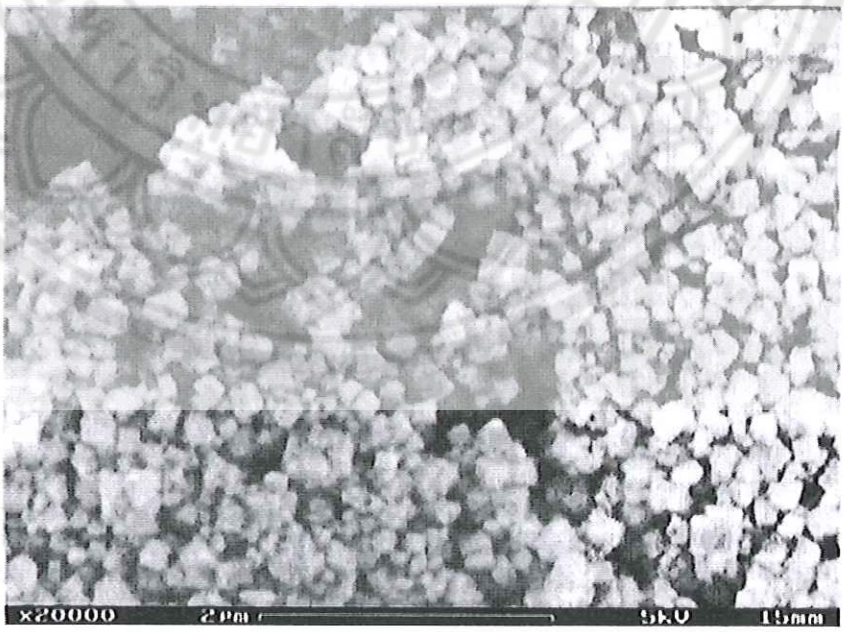

Figure 2.12 FESEM micrograph of the BKT powders was studied by Lencka *et al.* [48].

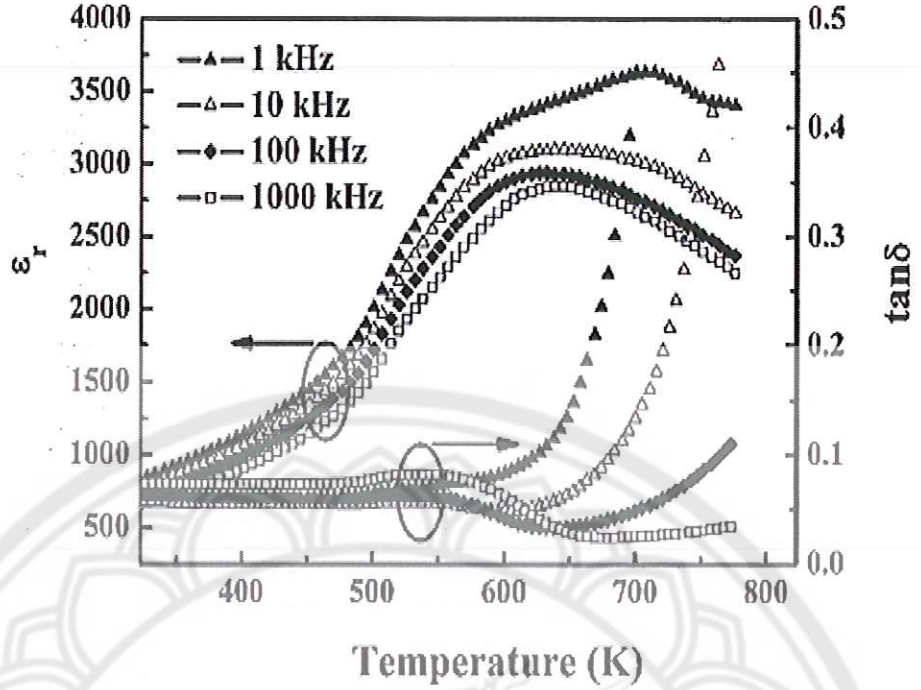

Figure 2.13 Temperature dependence of dielectric constant ε_r and loss tan δ at various frequencies for $(K_{0.5}Bi_{0.5})TiO_3$ ceramics [57].

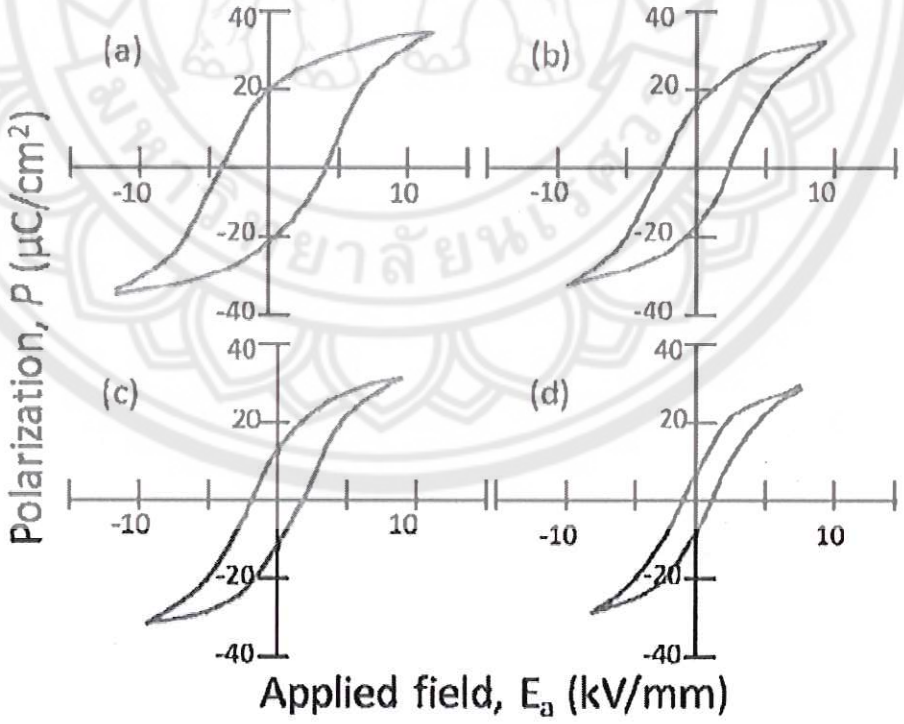

Figure 2.14 Polarization of KBT measured at temperatures of (a) 100 °C, (b) 200 °C, (c) 240 °C and (d) 260 °C [56].

2.3 Binary Systems

For some of the lead-free systems described above, the piezoelectric properties are enhanced through the use of dopants. The enhancement of piezoelectric properties is selection of a composition near an MPB in a solid solution. This section discusses the structure and properties of several lead-free binary solid solution material compositions.

2.3.1 $Bi_{0.5}Na_{0.5}TiO_3$ –$BaTiO_3$ (BNT-BT)

$BaTiO_3$ (BT) has also been combined in a solid solution with BNT, in which case an MPB is found at 6-7 mol% BT between the ferroelectric rhombohedral and ferroelectric tetragonal phases, as shown in Figure 2.15. At this composition, the system exhibits improved properties relative to BNT, such as the piezoelectric constant (d_{33}=125 pC/N), coupling factor (k_p=20%), and dielectric constant (ε_r=580) [59].

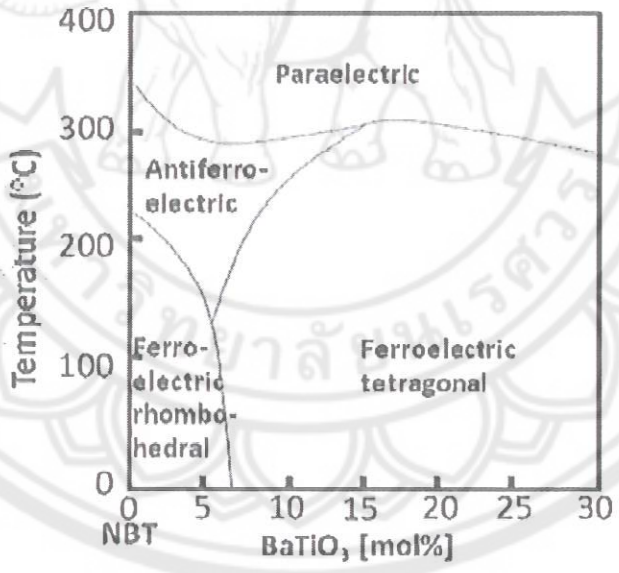

Figure 2.15 Phase diagram of BNT-BT showing the MPB between the ferroelectric rhombohedral phase and the ferroelectric tetragonal phase, reproduced from Takenaka *et al*. [59]

2.3.2 $Bi_{0.5}Na_{0.5}TiO_3$ –$NaNbO_3$ (BNT-NN)

BNT was also combined with $NaNbO_3$ (NN) by Li *et al* [6]. They reported that the solid solution of BNT-NN forms MPB between rhombohedral ferroelectric and orthorhombic anti-ferroelectric structure in the region of 2-8 mol% NN. At the MPB, the dielectric constant at RT, dielectric loss tangent at RT, piezoelectric constant and electro mechanical coupling factor varies from 467-889, 4.11-6.26 %, 31-88 pC/N and 12.3-17.9%. Furthermore, the BNT-NN ceramics exhibited relaxer behavior which is characterized by a diffused phase transition, as shown in Figure 2.16.

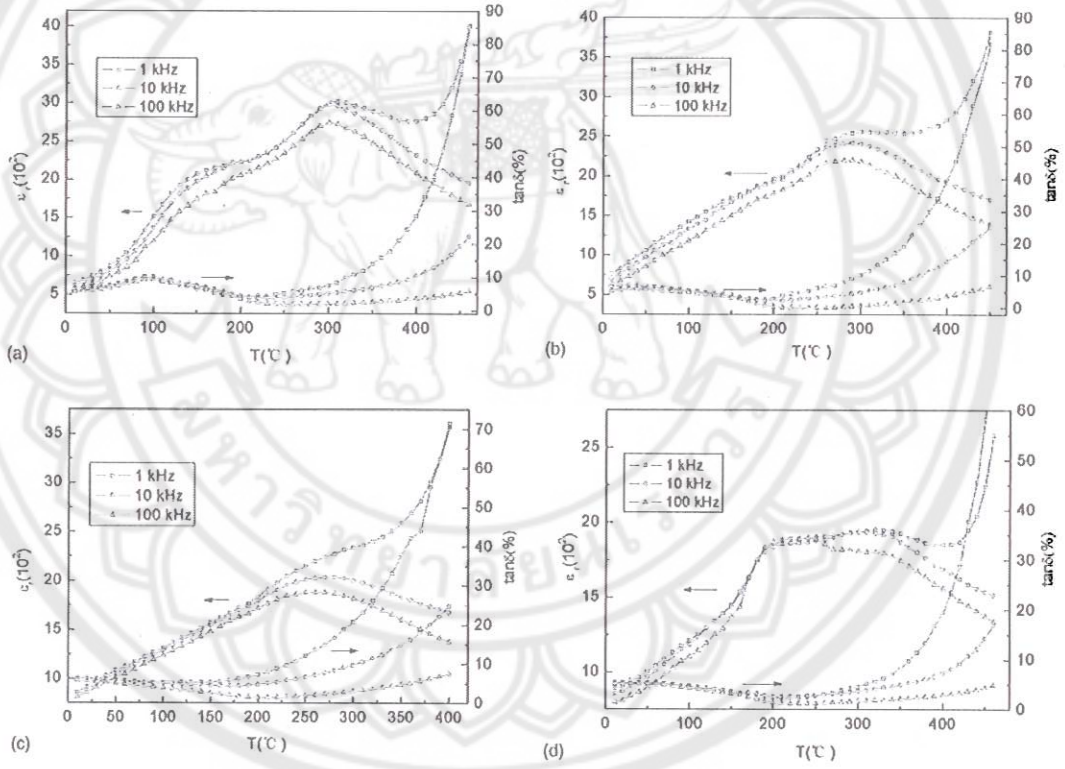

Figure 2.16. Temperature dependence of dielectric constant (ε_r) and dielectric loss (tanδ) for (1-x)NBT–xNN ceramics at 1, 10, 100 kHz with (a) x = 0.02, (b) x = 0.04,(c) x = 0.06, and (d) x = 0.08 [6].

2.3.3 $Bi_{0.5}Na_{0.5}TiO_3$ –$Ba(Cu_{0.5}W_{0.5})O_3$ (BNT-BCW)

For the BNT-BCW system, the structure remains a single rhombohedral phase with no MPB was seen within the addition amount of BCW from 0 to 6 mol%. The addition of BCW into BNT ceramics facilitated the poling process of a reduction in leakage current. 0.995BNT-0.005BCW ceramics exhibit a relatively high piezoelectric electric constant (d_{33}= 80 pC/N), electromechanical coupling factor (k_p=18.1%), dielectric constant (ε_r = 328) and a relatively low dielectric loss (tanδ = 0.015) [60].

2.3.4 $Bi_{0.5}Na_{0.5}TiO_3$ –$SrTiO_3$ (BNT-ST)

BNT was also combined with ST by watanabe *et al.* [7], showing an increase in the dielectric constant compared to undoped BNT, as shown in Figure 2.17. T_d, T_m and T_{R-T} of BNT-ST ceramics was found that it shifts the lower temperature when the ST content increased as shown in Figure 2.18. The optimum values of d_{33} is 133 pC/N obtained from 0.80BNT-0.20ST ceramics.

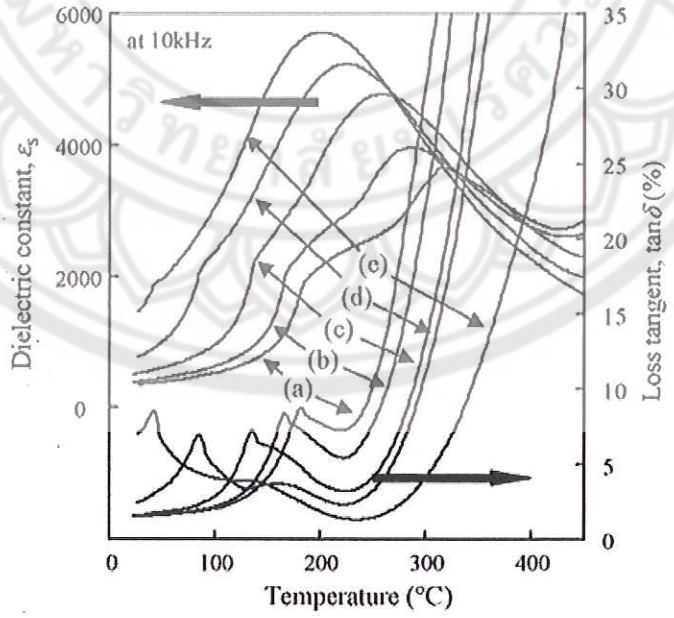

Figure 2.17 The dielectric constant and tanδ of BNT-ST (a) x = 0.04, (b) x = 0.08, (c) x = 0.14, (d) x = 0.20 and (e) x = 0.24 [7].

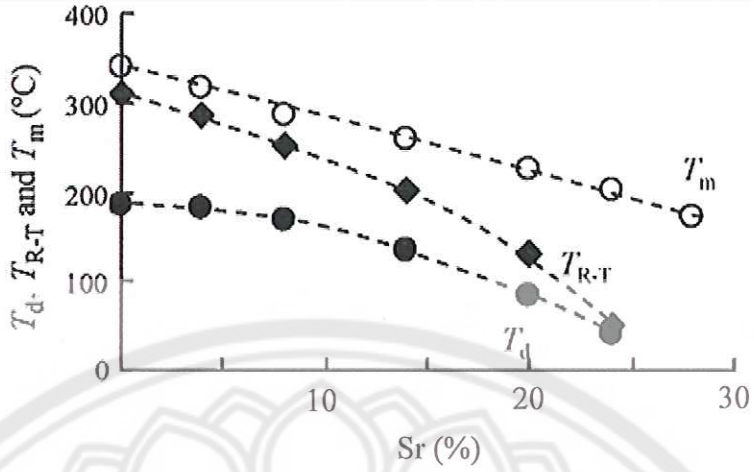

Figure 2.18 T_d, T_{R-T} and T_m of BNT-ST ceramics [7].

2.3.5 $Bi_{0.5}Na_{0.5}TiO_3$-$Bi_{0.5}K_{0.5}TiO_3$ (BNT-BKT)

The crystal structure of BNT-BKT ceramics was studied by Yang *et al.* [1]. They reported that a solid solution of BNT-BKT forms MPB between rhombohedral and tetragonal structure in the region of 16-22 mol % BKT. It agrees with the results of Sasaki [61]. The addition of BKT into BNT ceramic affected the grain size decrease. The density increases with increasing BKT content, the maximum density is obtained at 18 mol% of BKT, as shown in Figure 2.19.

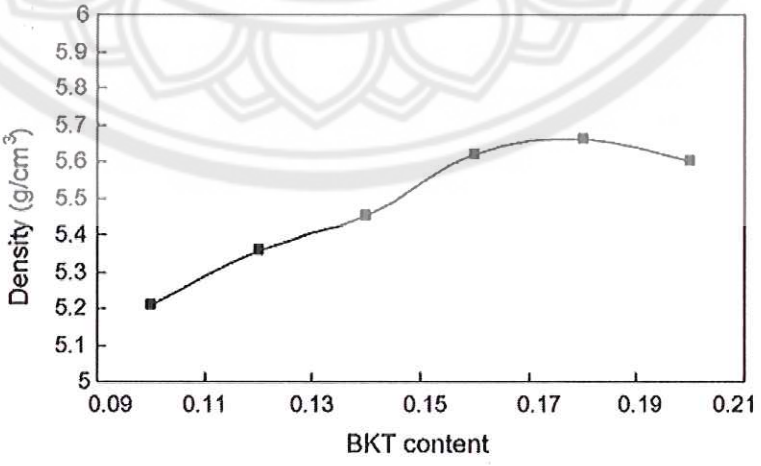

Figure 2.19 Density of BNT-BKT ceramics [1].

The dielectric constant (ε_r) and dielectric loss (loss tanδ) of BNT-BKT were also reported. The high concentration of caused the ε_r increases and the loss tanδ to decreased. There are two abnormal temperature peaks at around 100-200 and 300-350 °C were reported. Takenka *et al.* [62] concluded that these dielectric anomalies are attributed to ferroelectric-antiferroelectric and antiferroelectric-paraelectric phase transitions from the shape of P-E curve. Furthermore, BNT-BKT ceramics exhibited a relaxer ferroelectric behavior, as shown in Figure 2.20, agrees with the results of Yasuda and Konda [63].

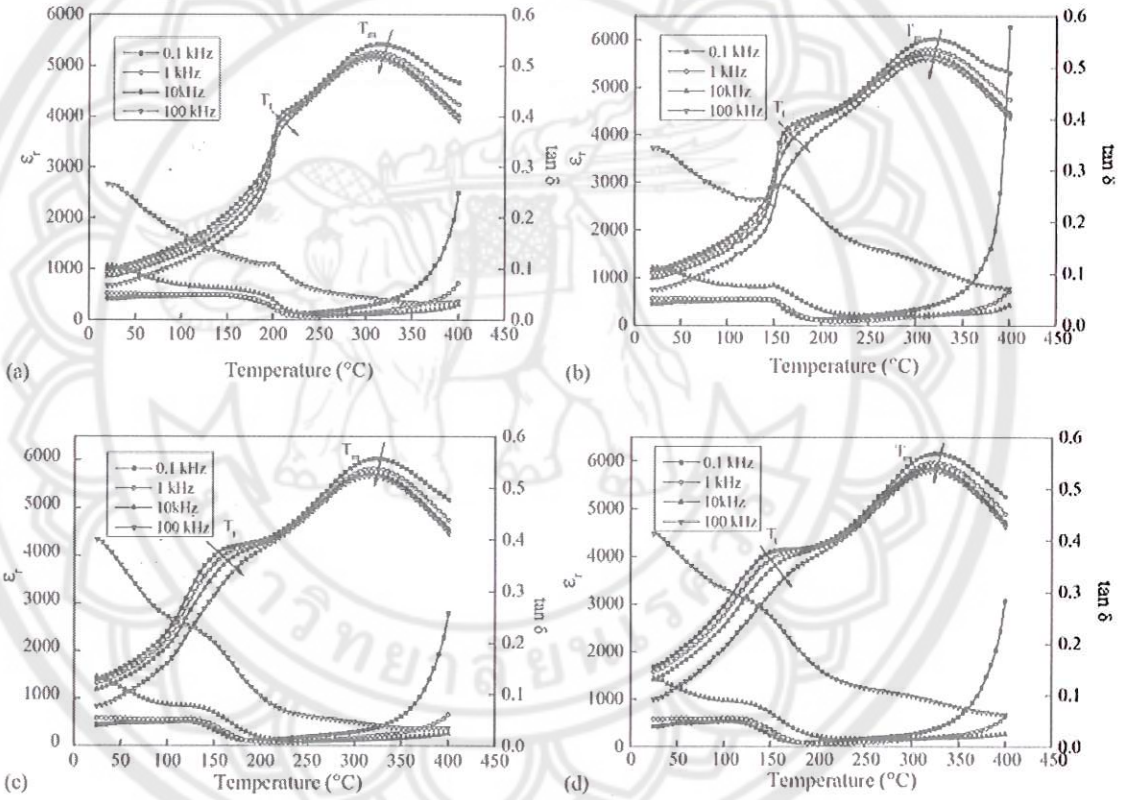

Figure 2.20 The dielectric constant and dielectric loss of BNT-BKT ceramics: (a) 12 mol% of BKT (b) 16 mol% of BKT (c) 18 mol% of BKT (d) 20 mol% of BKT [1].

The piezoelectric constant (d_{33}) and electromechanical coupling factor (k_p) of BNT-BKT were also reported. The addition of BKT into BNT ceramics increased d_{33} and k_p. The optimum values of d_{33} and k_p were found to be 144 pC/N, 29% at 18 mol% of BKT.

From the literature, the solid solution of BNT-BKT ceramics showed different piezoelectric properties. A comparison of the properties of BNT-BKT ceramics and BNT doping other of various groups is shown in Table 2.3.

Table 2.3 The optimal piezoelectric constant (d_{33}) and electromechanical coupling factor (k_p) of the composition in various BNT-based piezoelectric ceramics

BNT-based solid solution	MPB	d_{33} (μC/N)	K_p (%)	Ref.
BNT	-	58	12	[64]
$0.94BNT\text{-}0.06BaTiO_3$	o	125	20	[65]
$0.995BNT\text{-}0.005Ba(Cu_{0.5}W_{0.5})O_3$	o	80	18.1	[60]
$0.98BNT\text{-}0.02NaNbO_3$	-	88	17.9	[6]
$0.985BNT\text{-}0.01EuTiO_3$	-	46	-	[66]
$(Bi_{0.5}Na_{0.5})_{0.9742}La_{0.0172}TiO_3$	-	91	13	[67]
$0.98BNT\text{-}0.02BiScO_3$	-	74	14.4	[68]
$0.99BNT\text{-}0.01CaTiO_3$	-	50	13.8	[7]
$0.993BNT\text{-}0.007Bi(Mg_{2/3}Nb_{1/3})O_3$	-	94	-	[69]
$0.994BNT\text{-}0.006BaNb_2O_6$	-	94	-	[70]
$0.88BNT\text{-}0.12PbTiO_3$	o	106.6	33.2	[71]
$0.82BNT\text{-}0.18Bi_{0.5}K_{0.5}TiO_3$	o	144	29	[1]

2.4 Ternary Systems

As the binary systems described above still have many drawbacks and are not capable of replacing PZT in all of its applications, new lead-free compositions have become even more complex through the use of ternary solid solutions.

2.4.1 $Bi_{0.5}Na_{0.5}TiO_3$-$Bi_{0.5}K_{0.5}TiO_3$-$BiFeO_3$ (BNT-BKT-BF)

Several reports have been by Zhou *et al.* for the BNT-BKT-BF ternary system. The MPB in this system is between rhombohedral and tetragonal phases, where composition of $0.18<x<0.21$ and $0<y<0.05$ in (0.97-x)BNT-xBKT-0.03BF and (0.82-y)BNT-0.18BKT-yBF [18]. Zou *et al.* [72] studied the microstructure of BNT-BKT-BF ceramics by SEM technique. They reported that the addition of BF into BNT-BKT caused bulk sample increased and promote grain growth.

Measurement of the dielectric constant ε_r, piezoelectric constant d_{33} and the planar electromechanical coupling factor k_p of BNT-BKT-BF ceramics were studied by zhou *et al.* [19]. The ε_r, d_{33} and K_p increased with increasing BF into BNT-BKT ceramics. The ceramics were found to exhibit a typical relaxor behavior. 0.79BNT-0.18BKT-0.03BF ceramics demonstrated the largest d_{33} and k_p are 170 pCN^{-1} and 36.6 %, as shown in Figure 2.21 (a) and (b) and Figure 2.22, which shows that ceramics are very promising lead-free piezoelectric materials.

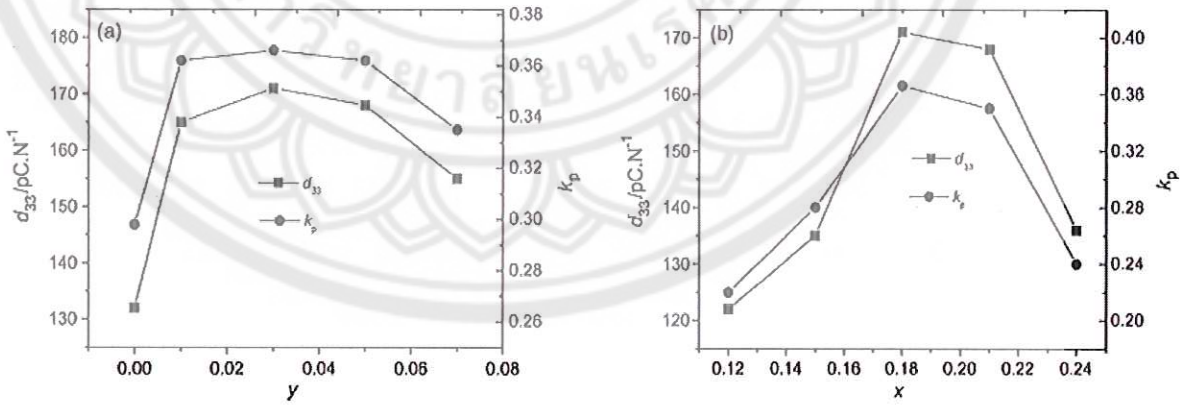

(a) (b)

Figure 2.21 Piezoelectric constant d_{33} and planar electromechanical coupling factor k_p of (1−x−y)BNT–xBKT–yBF ceramics as a function of the amount of BKT and BF: (a) x = 0.18 and (b) y = 0.03 [19].

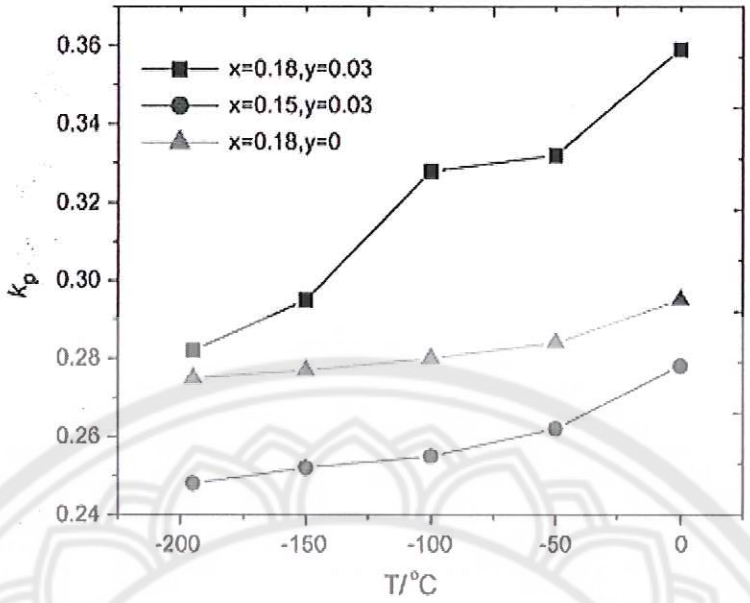

Figure 2.22 The electromechanical coupling factor k_p of (1−x−y)BNT–xBKT–yBF ceramics with x =0.18, y =0; x =0.18, y = 0.03 and x =0.15, y = 0.03 [19].

2.4.2 $Bi_{0.5}Na_{0.5}TiO_3$-$Bi_{0.5}K_{0.5}TiO_3$-$K_{0.5}Na_{0.5}Nb_{0.5}$ (BNT-BKT-KNN)

$K_{0.5}Na_{0.5}Nb_{0.5}$ (abbreviated as KNN) is a well-known lead-free piezoelectric ceramic because of its high Curie temperature ~420 °C and large electromechanical coupling factors. Recently, Yao *et al.* [15] added a small amount of KNN to BNT-BKT. The phase transition between rhombohedral and tetragonal phases was confirmed. The piezoelectric properties of BNT-BKT-KNN were also reported. 0.75 BNT-0.22BKT0.03KNN exhibited the d_{33} of 167 pC/N and k_p of 35.5%, as shown in Figure 2.23.

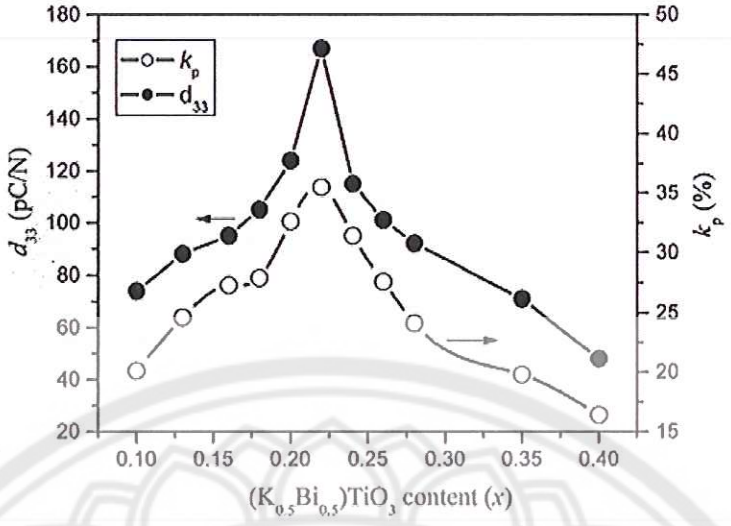

Figure 2.23 Piezoelectric coefficient d_{33} and planar coupling factor k_p of (1-x-y)BNT-xBKT-0.30KNN at x = 0.10–.40 [15].

Hussain *et al.* [73] studied the bipolar strain behavior of KNN-modified BNT-BKT measured at 0.2 Hz under an applied electric field of 50 kV/cm. They have shown BNT-BKT without KNN exhibit a butterfly-shaped curve typical of ferroelectric material with maximum and negative strains of 0.12% and 0.11%, respectively. When a small amount of KNN is introduced, the curves change shape, resulting in an increase in maximum strain and a concurrent decrease in the negative strain. At 3 mol% KNN, a significant enhancement in strain (S=0.22%). Singh *et al.* [74] studies the BNT-BKT-KNN ternary system by conventional solid state method. 0.80 BNT-0.20BKT0.01KNN exhibited the largest strain ever reported for a polycrystalline lead-free ceramics, ~0.80%, as shown in Figure 2.24, which is even higher than the strain obtained with established ferroelectric $Pb(Zr,Ti)O_3$ ceramics and is comparable to strains obtained in Pb-based antiferroelectrics.

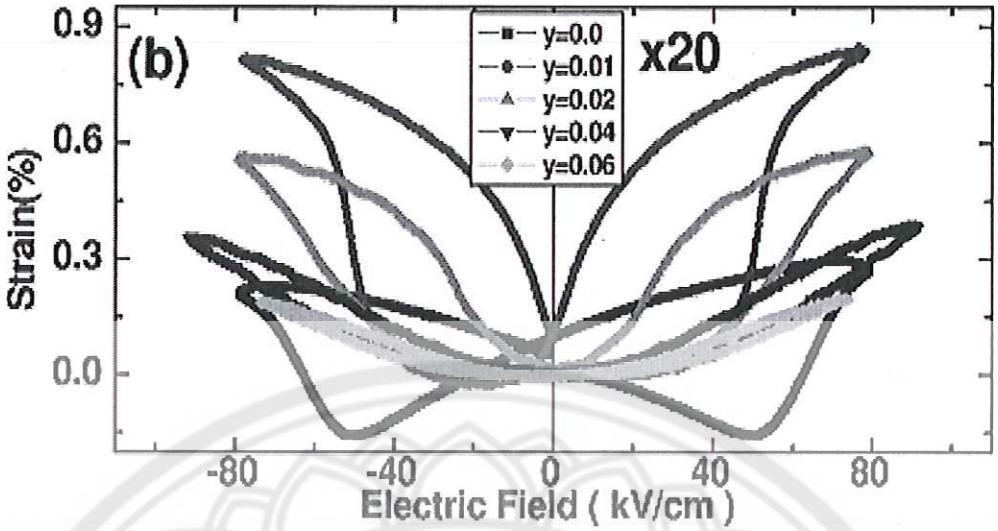

Figure 2.24 Bipolar strain vs electric field of 0.80BNT-0.20BKT0.01KNN ceramic at room temperature at 1 Hz [74].

2.4.3 $Bi_{0.5}Na_{0.5}TiO_3$-$Bi_{0.5}K_{0.5}TiO_3$-$Bi_{0.5}Li_{0.5}TiO_3$ (BNT-BKT-BLT)

Lin *et al.* [75] also studied the solid solution of BNT-BKT-BLT near the MPB. The ceramics were prepared by solid state reaction method and investigated by X-ray diffraction and piezoelectric properties. The XRD patterns showed the MPB of the rhombohedral phase and tetragonal phase. 0.70BNT-0.20BKT-0.10BLT demonstrated that the excellent piezoelectric constant and planar coupling factor of 231 pC/N and 41%, as shown in Figure 2.25. Hiruma *et al.* [76] added a small amount of KNN to BNT-BKT. The addition of BLT decreases greatly the sintering temperature and assists in the densification of BNT-BKT ceramics. The depolarization temperature (T_d) shows a strong dependence on the concentration of BLT and reaches the highest values at the MPB. This result shown that the BNT-BKT-BLT ceramics are promising candidates for the lead-free materials.

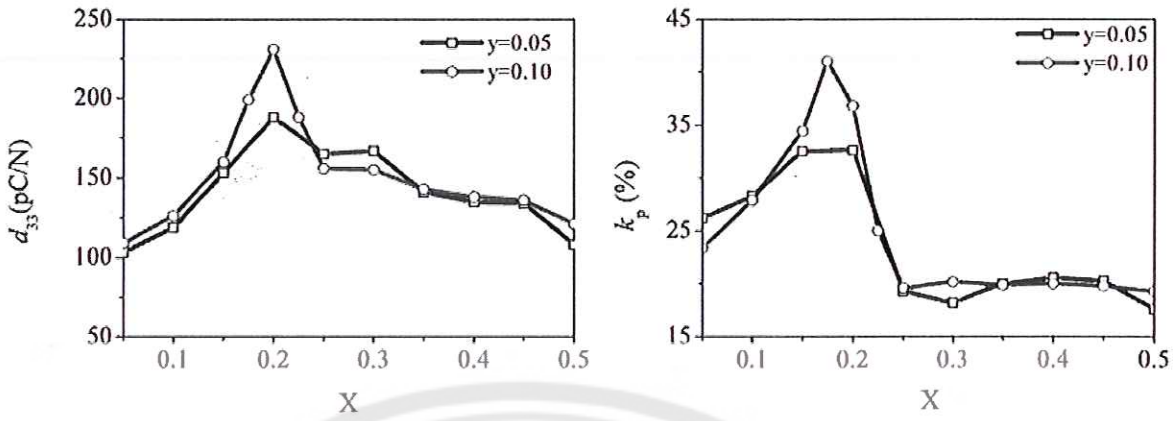

(a) (b)

Figure 2.25 Variation of piezoelectric coefficient d_{33} and planar electromechanical coupling factor kp with x for the (1-x-y)BNT-xBKT-yBLT ceramics (y=0.05 and 0.10) [75].

CHAPTER 3

EXPERIMENTAL PROCEDURES

In this chapter, the experimental procedures employed for preparation and characterization of BNT-BKT-based ceramics are described. The ternary system piezoelectric ceramics of $(1-x-y)(Bi_{1/2}Na_{1/2})TiO_3$-$x(Bi_{1/2}K_{1/2})TiO_3$-$yBiFeO_3$ with x=0.12-0.24; y=0-0.07 (abbreviated as BNKFT) are prepared in this work. The details are presented in the following sections.

3.1 Sample Preparation

Fabrications of materials, including powder preparation and ceramics fabrication have been employed as follow:

3.1.1 Powder Preparation

In 2002, Patil *et al.* [26] suggested the combustion method for synthesis of nanomaterials. The combustion method is characterized with self energy, short reaction times and low-cost method for production of various industrially useful materials. Some other advantages of combustion synthesis such as use of relatively simple equipment, formation of high-purity products, stabilization of detestable phases and formation of virtually any size and shape products. Therefore, the combustion method was chosen for preparation BNKFT powders.

3.1.1.1 Preparation of BNKFT powders

The ternary system of $(1-x-y)Bi_{0.5}Na_{0.5}TiO_3–xBi_{0.5}K_{0.5}TiO_3–yBiFeO_3$ with x= 0.12-0.24 y=0-0.07 was synthesized by combustion method. Reagent grade Bi_2O_3, $NaCO_3$, TiO_2, Fe_2O_3, K_2CO_3 were used as starting materials. The details of these oxides; such as the supplier, formula weights and purities, are listed in Table 3.1. First, these oxides or carbonate powders were weighed in appropriate stoichiometry. The ball-milling technique was employed for the mixing and milling in this work. The powders were mixed by ball milling for 24 h. with ethanol as a solution media. Drying was carried out on a hotplate with a magnetic stirring until the mixture nearly dry, and then placed in a 120 °C drying oven for 2 h. The suspensions were dried and the powders were ground using an agate mortar and then sieved into a fine powder. The mixed powders and glycine ($C_2H_5NO_2$) were mixed with a ratio of 1:2 in an agate mortar. The BNKFT powders were then calcined at various temperatures until the optimum condition was determined. The mixing process of BNKFT powders are shown in the form of diagram in Figure 3.1 respectively. The calcined powders were analyzed by X-ray diffraction technique to determine the amount of the perovskite phase percentage.

Table 3.1 Specifications of starting materials used in this study.

Materials	Source	Formula weight	Purity (%)
Bi_2O_3	Qrec	208.98	99.5%
$NaCO_3$	Riedel-de Haën	22.99	99.5%
TiO_2	Sigma-Aldrich	47.90	99.5%
Fe_2O_3	Riedel-de Haën	55.85	97.0%
K_2CO_3	Riedel-de Haën	39.10	98.0%

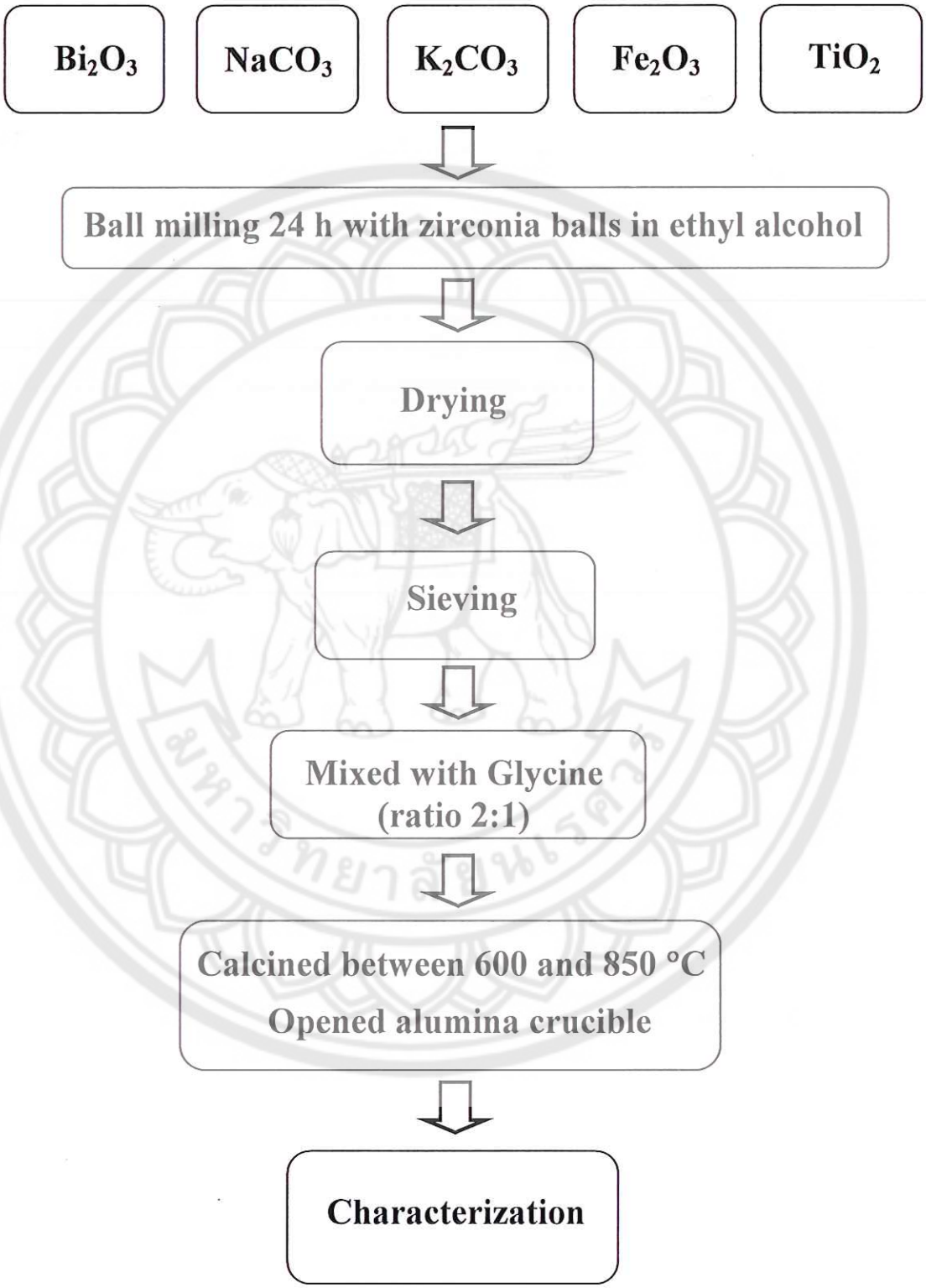

Figure 3.1 Diagram of experimental procedure on BNKFT powder preparation.

3.1.2. Ceramic Preparation

The calcined powders received from the processes described in previous sections were mixed with 3 wt.% polyvinyl alcohol (PVA, Fluka) which used as binder. The mixing powders were pressed by uniaxial hydraulic to form disc-shaped pellets 10 mm in diameter. Binder was burn out on sintering step at temperature 500 °C for 1 h. The green pellets were placed on the alumina powders-bed inside alumina crucible, before insertion into a high temperature furnace.

3.2 Sample Characterization

All powders and ceramics were characterized using different tools as described below in Figure 3.2.

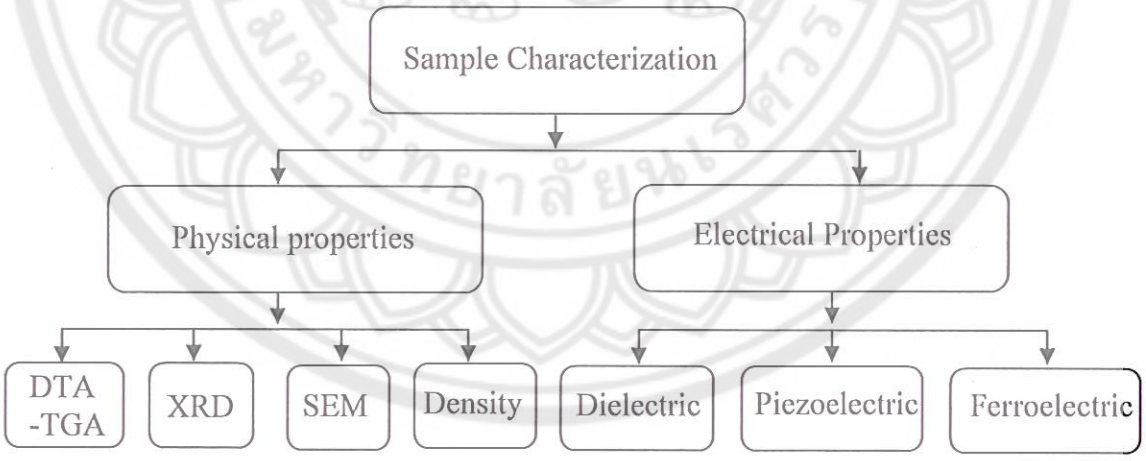

Figure 3.2 Diagram of experimental procedure on sample characterization.

3.2.1 Physical properties

3.2.1.1 Thermogravimetric and Differential Thermal Analysis (TGA-DTA)

Thermogravimetric and Differential Thermal Analysis (TGA-DTA) techniques were employed for investigation of thermal behavior of the uncalcined powders. The thermal decomposition and weight loss behavior of the uncalcined powders were carried out by a thermalgravimetric analyzer (TGA) and differential thermal analyzer (DTA). The uncalcined powder were heated from room temperature up to 1300 °C in platinum crucible, with reference powder of Al_2O_3 and a heating rate of 10 °C/min.

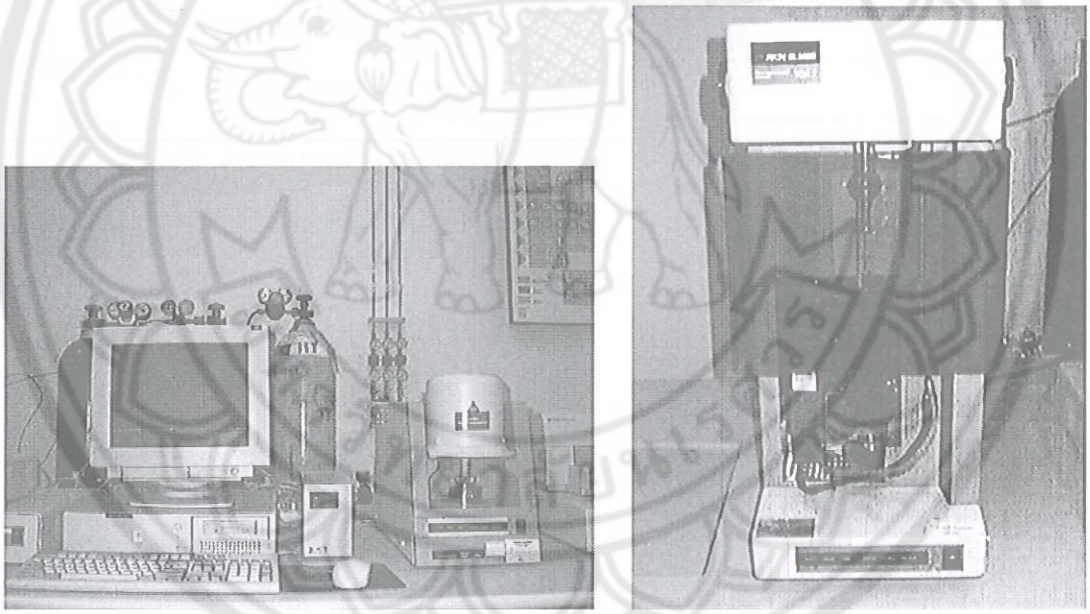

(a) (b)

Figure 3.3 Thermal analyzer: (a) TGA and (b) DTA.

3.2.1.2 X-ray diffraction (XRD) Technique

The X-ray diffraction (XRD) was used to analyze phase formation and phase purity which was especially important in minimizing pyrochlore phase formation in BNT-BKT based compounds of the powders and pellets. The room temperature XRD patterns were recorded with a Siemens-D500 diffractometer at Naresuan University with Cu Kα radiation at 20 kV, shown as Figure 3.6. The relative amounts of the perovskite and pyrochlore phases were estimated from these major peak intensities (110) or the respectively phases. The estimation was suggested by Swartz and Shrout [75] using the following equation:

$$\%\ perovskite\ phase = \left(\frac{I_{perov}}{I_{perov} + I_{Pyr}} \right) \times 100 \qquad (3.1)$$

This well-known equation is widely employed in connection with the preparation of complex perovskite structure materials. I_{perov} referred to the intensity of the (110) perovskite peak, intensities of the highest, I_{pyr} peaks.

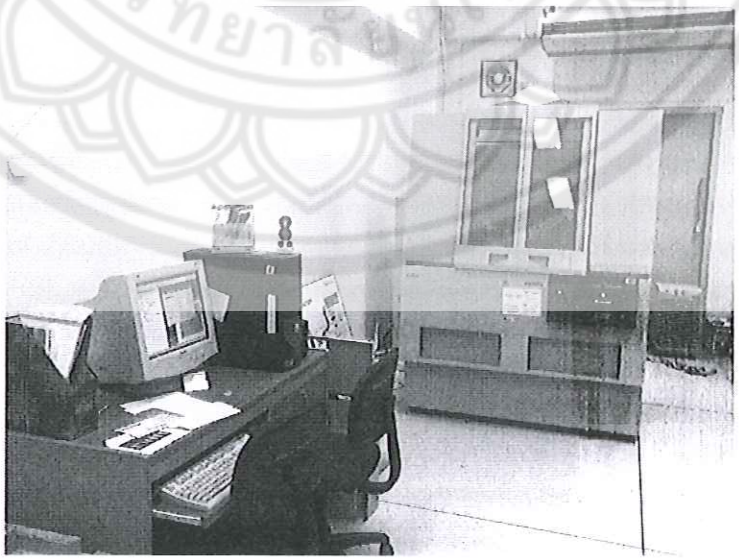

Figure 3.4 X-ray diffractometer.

3.2.1.3 Scanning Electron Microscopy (SEM)

Microstructural characterization of sample surface using scanning electron microscopy (SEM) was used to determine the grain size and the presence of porosity, as shown in Figure 3.7. Average grain size of the sintered ceramics were estimated by using a linear intercepting method [76], where random lines were drawn on a micrograph and the number of grain boundaries intercepting these lines were then counted.

Figure 3.5 Scanning electron microscope (SEM).

3.2.1.4 Densification Measurement

The densities of all compositions of both systems were determined by a method based on the Archimedes principle. Initially, the samples were weight dry (W_1), then weighted again after fluid impregnation (W_2), and finally weight while being immersed in water (W_3). Density of each sample was calculated by following equation [77]:

$$\rho_c = \frac{W_1 \rho_w}{W_2 - W_3} \tag{3.2}$$

where, is the density of water at room temperature (g/cm^3) and is the density of sample at room temperature (g/cm^3); however the density of water is slightly temperature dependent as

3.2.2 Electrical properties

3.2.2.1 Dielectric Measurement

The dielectric properties of the sintered ceramics were studied as functions of both temperature and frequency with an automated dielectric measurement system in Figure 3.8. The computer-controlled dielectric measurement system consists of a precision LCR-meter (Agilent 4263B), a temperature chamber, and a computer system. The capacitance and the dielectric loss tangent are determined over the temperature range of 50 and 500 °C with the frequency at 10 kHz.

The dielectric constant was calculated by equation,

$$\varepsilon_r = \frac{Ct}{\varepsilon_0 A} \tag{3.3}$$

where ε_r and ε_0 are the dielectric constant and permittivity of free space. C is the capacitance, and t and A are the thickness and area of the sample.

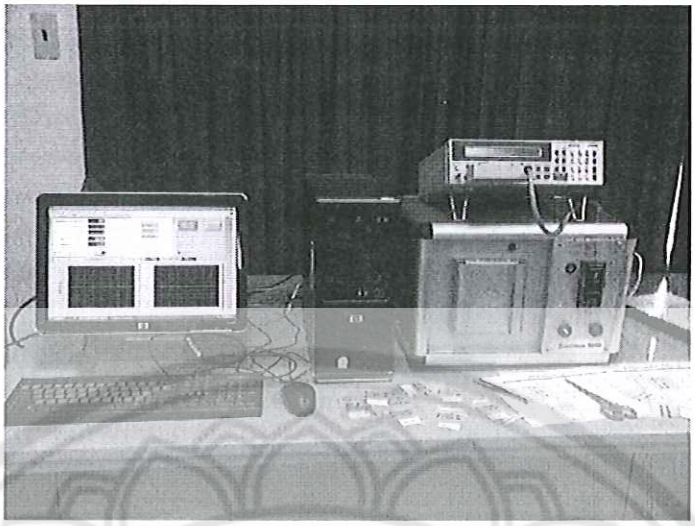

Figure 3.6 Dielectric Measurements system.

3.2.2.2 Hysteresis properties measurement

To measurement hysteresis properties, a modified Sawyer-Tower circuit was employed. The experiment set up was designed to measure the sample's response under external electric fields. Sinusoidal signals generated by a signal generator (model GAG-809, Good well instrument. CO.LTD) were amplified and applied to the sample and to a standard capacitor in series. The voltage (V_y) developed on the standard capacitor, due to the polarization of the sample, was fed to the Y-axis (or V_y) of an X-Y scope in 12-bit PC-Oscilloscope (Picoscope) on computer. The electric field, measured on the X-axis (or V_x), was also fed to the computer. All measurements were carried out at room temperature at a fixed frequency of 50 Hz.

For each measurement, the ceramic was placed in the sample holder, which was submerged in silicone oil to prevent on electric breakdown. The sample was connected to the standard capacitor on a modified Sawyer-Tower circuit. The sample could be considered as a capacitor (C_s) connected in series to the standard capacitor

(C0). Since the capacitance of the sample was much smaller than that of the standard capacitor, almost all of the electric potential of the high voltage source acts on the samples.

By definition, polarization is the value of dipole moment per unit volume or amount of charge accumulated per unit surface area. Polarization of the sample induces by electric fields loading, P_{sample} was given by

$$P_{sample} \frac{Q_s}{A} \tag{3.4}$$

where, Q_s is the amount of charges accumulated on the electrode of the sample

A is the area of the electrode of the sample

Since the reference capacitor was connected in series to the sample, the amount of charges are equivalent:

$$Q_s = Q_0 \tag{3.5}$$

where, Q_0 is the amount of charges accumulated on the standard capacitor.

On the other hand, the amount of charges on the standard capacitor is equal to

$$Q_0 = V_y C_0 \tag{3.6}$$

where, V_y is the voltage across the standard capacitor, $C_0 = 0.1\mu F$, is the capacitance of the standard capacitor.

Then the polarization induced by electric field loading could be calculated as

$$P_{sample} = \frac{V_y C_0}{A} \tag{3.7}$$

Consequently, by monitoring the voltage across the standard capacitor, the polarization of the sample could be determined.

From the X-axis of the monitor of oscilloscope, the electric field was calculated using the following equation:

$$E = \frac{V_x}{d} \tag{3.8}$$

where, V_x is the voltage across the sample

d is the thickness of the sample

3.2.2.3 Piezoelectric properties measurement

The optimum poling conditions were determined by poling the ceramics with applying DC field of 30kV/cm in a stirred oil bath at 150 °C for a time period 30 minutes. The piezoelectric constant (d_{33}) was measured using a quasi-static piezoelectric d_{33} meter. The piezoelectric constant (d_{33}) measurements were made directly after poling and after 24 hours. Measurements were conducted at a drive frequency of 100 Hz.

CHAPTER 4
RESULTS AND DISCUSION

In this chapter, the results are presented on both powder and ceramic form of $(1-x-y)Bi_{0.5}Na_{0.5}TiO_3$–$xBi_{0.5}K_{0.5}TiO_3$–$yBiFeO_3$ (BNKFT), including microstructural, densification of materials and local structure analysis. Results of electrical properties, piezoelectric properties, ferroelectric hysteresis loop (*P-E* loop) and dielectric properties, of the materials are also presented.

4.1 Effect of calcination temperature and content of *x* and *y* on crystal structure and microstructure of BNKFT powders

The XRD patterns of BNKFT0.12/0.03 and BNKFT0.18/0.01 calcined powders at various temperatures are shown in Fig 4.1(a) and Fig 4.1(b), respectively. The X-ray analysis indicated that BNKFT0.12/0.03 and BNKFT0.01/0.18 calcined from 600 °C to 800 °C, had mainly a set peak with a major peak at (110). The crystal structure belonged to a rhombohedral phase, which could be matched with JCPDS file number 360340. The impurity phase of $K_4Ti_3O_8$ was found in the BNKFT0.12/0.03 and BNKFT0.01/0.18 powders calcined below 750 °C. Above 750 °C the impurity phase disappeared and the sample showed a pure perovskite phase. The results of BNKFT0.15/0.03, BNKFT0.18/0.03, BNKFT0.21/0.03, BNKFT0.24/0.03, BNKFT0/0.18, BNKFT0.01/0.18, BNKFT0.03/0.18, BNKFT0.05/0.18 and BNKFT0.07/0.18 were similar to BNKFT0.12/0.03 and BNKFT0.18/0.01. The relative amounts of the perovskite phase were calculated by measuring major peak intensities of the perovskite phase. The percentage of perovskite is described by the following equation:

$$\%\ Perovskite\ phase\ =\ \left(\frac{I_{Perov}}{I_{Perov}+I_{K_4Ti_3O_8}}\right)\times 100 \qquad (4.1)$$

This well-known equation is widely employed in connection with the preparation of complex perovskite structure materials. I_{perov} and $I_{K_4Ti_3O_8}$ are the intensity of the (110) perovskite and the intensity of the highest $K_4Ti_3O_8$ peak. The percent of the perovskite phase of BNKFT-*x*/0.03 and BNKFT-0.18/*y* powders at various calcination temperatures was calculated and is listed in Table 4.1. The percentage of the perovskite phase in all samples increased with an increase of the calcination temperatures and the highest percentage was observed in powders calcined above 750 °C. The lattice parameter *a* of BNKFT-*x*/0.03 and BNKFT-0.18/*y* powders at different calcined temperatures (600 °C-800 °C) were calculated from the (101), (012), (110), (003), (021), (202), (113), (211), (104) and (122) reflective peaks of XRD patterns and are listed in Table 4.1.

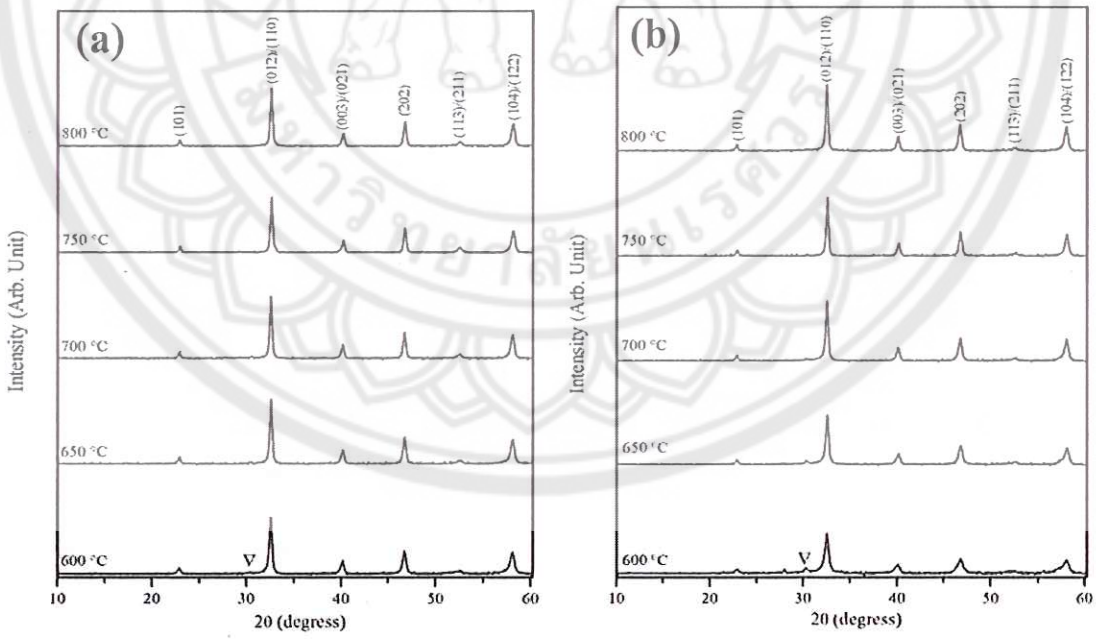

Fig. 4.1. XRD patterns of (a) BNKFT0.12/0.03 and (b) BNKFT0.18/0.01 powders calcined at various temperatures for 2 h: (∇ $K_4Ti_3O_8$).

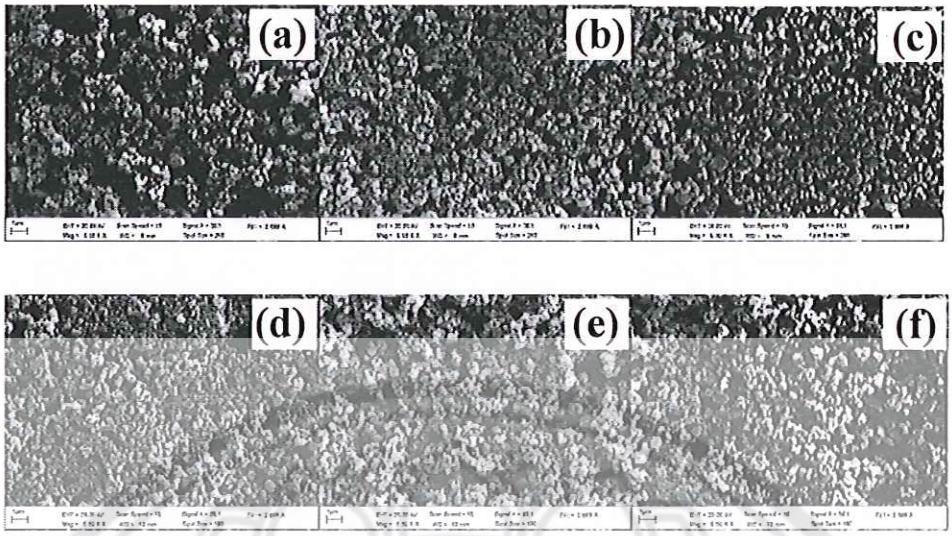

Fig. 4.2. SEM photomicrographs of BNKFT-0.12/0.03 calcined at (a) x=600°C, (b) 700°C, (c) 800°C and BNKFT- 0.18/0.01 calcined at (a) x=600°C, (b) 700°C, (c) 800°C.

The lattice parameter *a* of all the samples increased with an increase of calcinations temperature. It was observed that at low calcining temperatures, the powders exist in a more strained form within the atomic entities in non-equilibrium positions, which relax to the equilibrium positions at higher temperature. It may also be that the domain mobility is restricted due to pinning of the domain boundaries by crystal defects.

Fig. 4.2(a–f) shows SEM photomicrographs of BNKFT-0.12/0.03 and BNKFT- 0.18/0.01 powders at different temperatures. In general, the particles are agglomerated and have a spherical morphologic shape. With an increase of calcination temperatures from 600 °C to 800 °C, the average primary particle size increase from 264 nm to 411 nm (for BNKFT-0.12/0.03) and 228 nm to 328 nm (for BNKFT-0.18/0.01), and the agglomeration measured from 493 nm to 691nm (for BNKFT-0.12/0.03) and 467 nm to 673 nm (for BNKFT-0.18/0.01), as seen in Fig. 4.2(a–f) and listed in Table 4.1. It is also of interest to point out that average particle size tended to increase with increased calcination temperatures. This is because of the occurrence of hard agglomeration with a strong inter-particle bond within each aggregate which is the result of the firing process. The SEM

results of BNKFT-0.15/0.03, BNKFT-0.18/0.03, BNKFT-0.21/0.03, BNKFT-0.24/0.03, BNKFT-0/0.18, BNKFT-0.03/0.18, BNKFT-0.05/0.18 and BNKFT-0.07/0.18 were similar to BNTFT-0.12/0.03 and BNKFT-0.18/0.01, as listed in Table 4.1.

The optimum calcination temperature of all samples was found at 750 °C for 2 h, and it was then that the amounts of *x* and *y* on the crystal structure and microstructure were examined. The XRD diffraction patterns of BNKFT-x/0.03 and BNKFT 0.18-y powders in the range of 10°–60° are shown in Fig. 4.3(a) and 4.3(b), respectively. It has been verified that all the samples are of a single-phase perovskite structure. All the peaks of the solid solution system were indexed to the rhombohedral structure and the pattern matching based on JCPDS file no. 36-0340. The position corresponding to the characteristic (110) peak shifts towards a lower angle as the x and y content are increased in the solid solution, as shown in Fig. 4.3(a) and 4.3(b). The lattice parameter of *a* increased with increasing x and y content, as listed in Table 4.2. It is because the higher radius (1.64 Å) of the K^+ ion

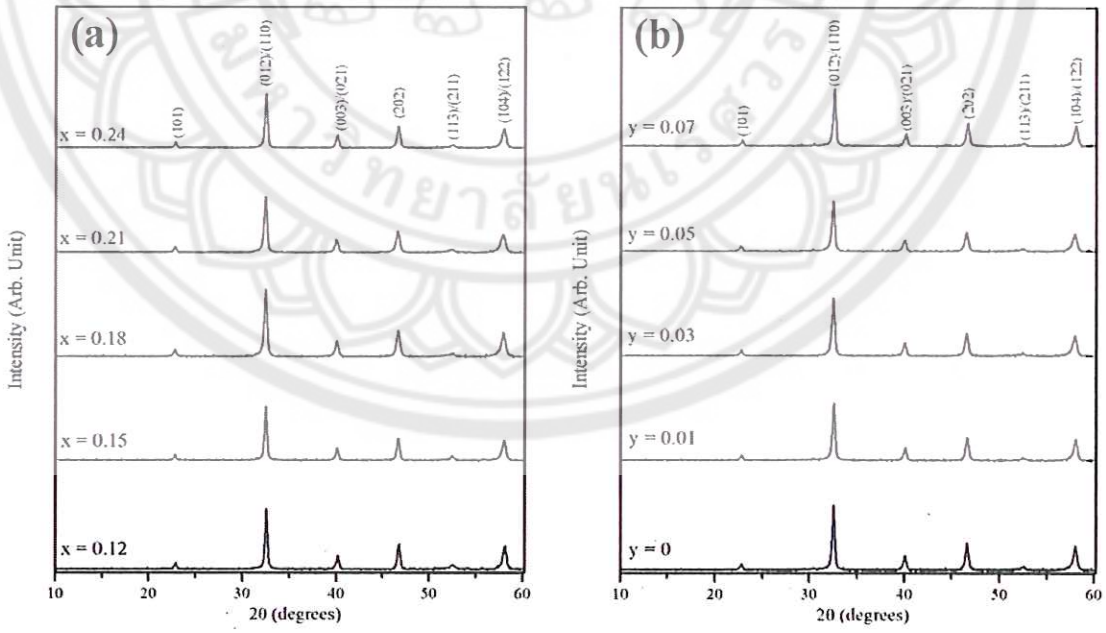

Fig. 4.3. X-ray diffraction patterns of (a) BNKFT-x/0.03 and (b) BNKFT 0.18/y calcined powders.

replaces Na^{+} (1.39 Å) and (0.65 Å) of the Fe^{3+} replaces Ti^{4+} (0.61 Å) resulting in the increase of the effective ionic radius of the A- and B-site respectively. The distortion of the unit cell induces strain in the lattice that may induce an increase of lattice parameter *a*.

The SEM micrographs of BNKFT-x/0.03 and BNKFT 0.18/y powders are exhibited in Fig. 4.4(a–c) and 4.4(d–f), respectively. All the particles are spherical in shape and agglomerated. With an increase of x content from 0.12 to 0.24, the average particle size decreases from 390 nm to 277 nm (Table 4.2). As the y content increased, the average particle size increased from 285 nm to 310 nm (Table 4.2).

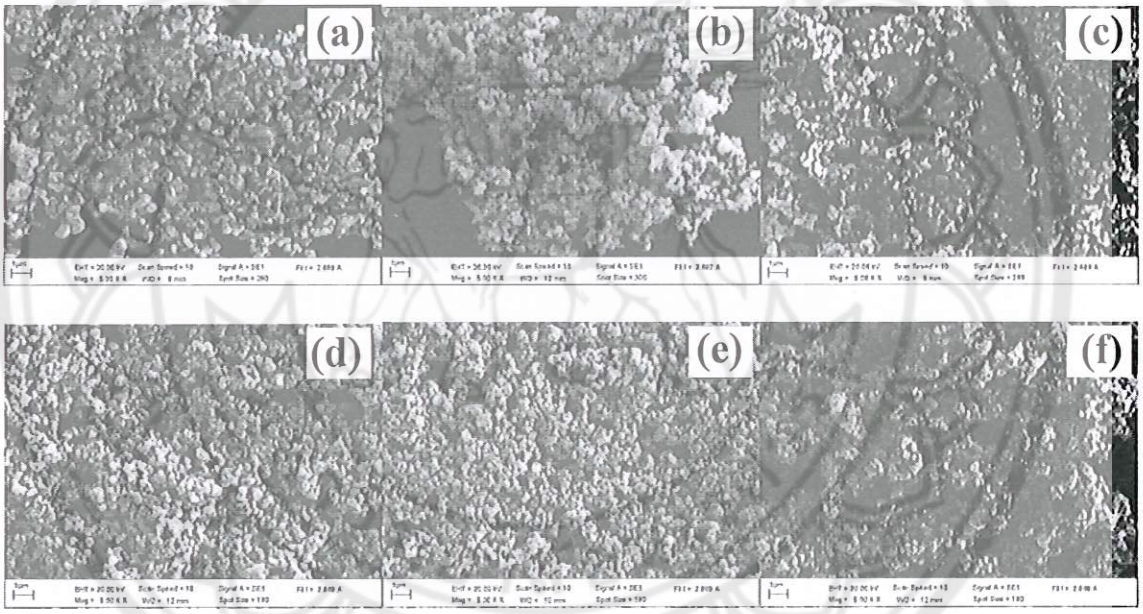

Fig. 4.4. SEM images of BNKFT-x/0.03 calcined powder with (a) x=0.12, (b) x=0.18, (c) x=0.24 and BNKFT 0.18/y calcined powder with (d) y=0, (e) y=0.03, (f) y=0.07.

The TEM micrographs of BNKFT-x/0.03 and BNKFT 0.18/y powders are shown in Fig. 4.5(a–c) and 4.5(d–f), respectively. It can be seen that the powder particles have a similar spherical shape and a porous agglomerated form. With an increase of the *x* content from 0.12 to 0.24, the average particle size decreased from 197 nm to 92 nm. The average particle size increased from 189 nm to 244 nm with an increase of the *y* content. However,

the TEM results were different in their values when compared with the particle size from the SEM image. This may have been caused by the agglomeration affects in the SEM results.

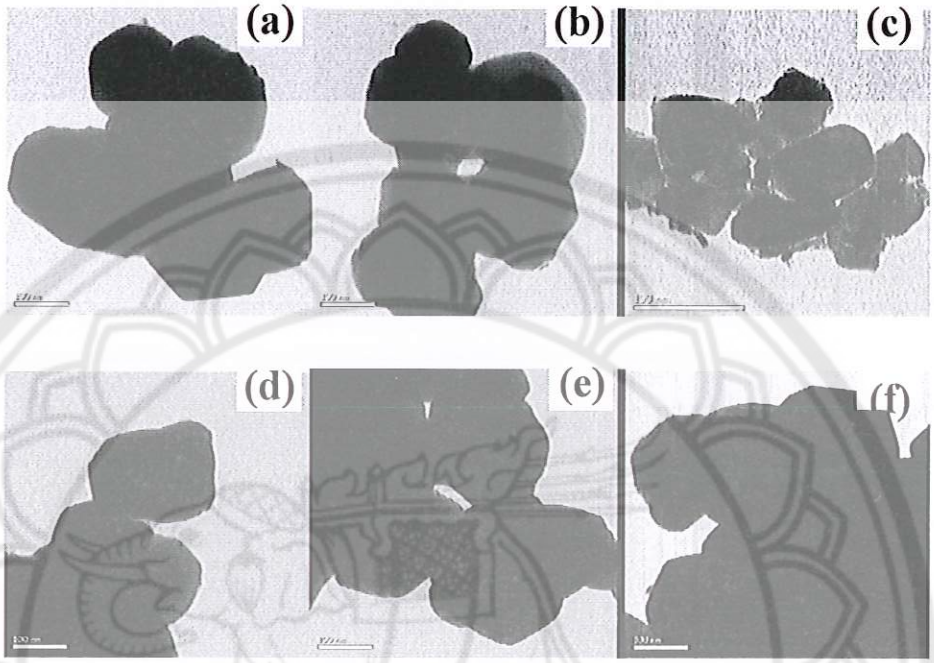

Fig. 4.6. TEM images of BNKFT-x/0.03 calcined powder with (a) x=0.12, (b) x=0.18, (c) x=0.24 and BNKFT 0.18/y calcined powder with (d) y=0, (e) y=0.03, (f) y=0.07.

Table 4.1. Perovskite phase, lattice parameter and average particle size of BNKFT-x/0.03 powders calcined at various temperatures

Composition of x	Calcination temperature (°C)	Perovskite phase (%)	Lattice parameter a (Å)	Average particle size (nm)
0.12	600	87.3	3.8332	264±0.058
	650	92.7	3.8371	277±0.088
	700	97.2	3.8376	297±0.092
	750	100	3.8415	390±0.150
	800	100	3.8442	411±0.167
0.15	600	96.5	3.8591	259±0.085
	650	95.0	3.8597	266±0.092
	700	95.9	3.8598	317±0.079
	750	100	3.8602	296±0.140
	800	100	3.8618	324±0.084
0.18	600	85.6	3.8562	236±0.077
	650	96.4	3.8579	269±0.079
	700	96.9	3.8590	271±0.104
	750	100	3.8617	300±0.096
	800	100	3.8628	309±0.071
0.21	600	95.0	3.8559	221±0.114
	650	97.4	3.8560	230±0.102
	700	98.0	3.8581	255±0.096
	750	100	3.8658	290±0.010
	800	100	3.8659	397±0.075
0.24	600	97.6	3.8545	210±0.078
	650	98.8	3.8575	233±0.096
	700	99.5	3.8624	260±0.088
	750	100	3.8696	277±0.080
	800	100	3.8698	283±0.104

Table 4.2. Perovskite phase, lattice parameter and average particle size of BNKFT-x/0.03 powders calcined at various temperatures

Composition of y	Calcination temperature (°C)	Perovskite phase (%)	Lacttice parameter a (Å)	Average particle size (nm)
0	600	83.5	3.8112	231±0.084
	650	93.2	3.8276	231±0.092
	700	96.2	3.8262	255±0.085
	750	100	3.8378	285±0.096
	800	100	3.8402	293±0.088
0.01	600	80.8	3.8208	228±0.076
	650	92.7	3.8486	260±0.077
	700	97.2	3.8562	291±0.112
	750	100	3.8611	296±0.092
	800	100	3.8694	328±0.097
0.03	600	85.6	3.8562	236±0.077
	650	96.4	3.8579	269±0.079
	700	96.9	3.8590	271±0.104
	750	100	3.8617	300±0.096
	800	100	3.8628	309±0.071
0.05	600	86.1	3.8697	216±0.090
	650	91.8	3.8712	235±0.114
	700	96.2	3.8864	262±0.107
	750	100	3.8802	308±0.099
	800	100	3.8802	309±0.123
0.07	600	80	3.8914	236±0.088
	650	89.9	3.8864	251±0.085
	700	96.5	3.9008	273±0.101
	750	100	3.9013	310±0.098
	800	100	3.9216	315±0.058

Table 4.3. Average grain size, density and shrinkage of BNKFT ceramics at various temperatures

Sintering temperature	Average grain size (μ)	Measured density (g/cm^{-3})	Relative density (%)	Shrinkage (%)
900	0.37	4.96	82.0	10.9
950	0.49	5.22	86.3	12.3
1000	1.21	5.47	90.4	16.9
1025	1.41	5.77	95.4	17.4
1050	1.59	5.85	96.9	18.0
1075	2.49	5.80	95.8	17.9

4.2 Effects of Sintering Temperature and amount of x and y on Crystal Structure and Microstructure of BNKFT ceramics

The XRD diffraction pattern of BNKFT0.18/0.03 sintered ceramics at various temperatures are shown in Fig. 4.7. The X-ray analysis indicated that BNKFT0.18/0.03 sintered 900 °C to 1075 °C. It can be seen that the BNKFT0.18/0.03 ceramics possess a single-phase perovskite structure in all samples. All the peaks of the solid solution system were indexed by pattern matching based on JCPDS data on BNT (36-0340) and $Bi_{0.5}K_{0.5}TiO_3$ (36-0339). Generally, the tetragonal structure is characterized by a single peak of (111) between 39 ° and 41° and (002)/(200) peaks splitting between 45° and 48°. Nevertheless, the rhombohedral structure is characterized by (003)/(021) peaks splitting between 39° and 41° and a single peak of (202) between 45° and 48°. At a sintering temperature of 900 °C, the (003)/(021) peaks splitting appears in the 2θ range of 39-41° (Fig. 4.7(b)) and the (202) peak is asymmetric in the range of 45-48° (Fig. 4.7(c)). When sintering temperature is increased, the (003)/(021) peak begins to merge into a single (111) peak and the (202) peak starts to split into two peaks of (002)/(200). These results revealed that the crystalline structure has

two phases between rhombohedral and tetragonal coexisting and also indicated that the sintering temperature affects the increase of the tetragonal and the decrease of the rhombohedral phases.

The SEM photographs of BNKFT0.18/0.03 sintered ceramics at various temperatures are shown in Fig 4.8. It was found that increasing sintering temperature helped the growth of grain size. The average grain size increased from 0.37 to 2.49 μm as listed in Table 4.3. A porous microstructure with small grain size was observed at 950 °C. The increase of sintering temperature significantly encouraged the grain growth and microstructure densification. However, the grain size of the sample sintered above 1050 °C also displayed a high degree of porosity. Moreover, the cross-section microstructure of the samples presented predominantly an inter-granular cleavage with sintering temperature below 1000 °C. At above 1000 °C, the samples changed from inter-granular to intra-granular. This indicated that the sintering temperatures strongly affect grain boundaries.

The density and shrinkage of BNKFT ceramics with sintering temperatures between 900 °C and 1075 °C can also be seen in Table 4.3. The density and shrinkage increased with increasing sintering temperatures from 900 °C to 1050 °C, and reached a maximum value of 5.85 g/cm^3 (96.9% of theoretical density) and 18.0% at 1050 °C and decreased after further sintering at a higher temperature (1075 °C). The decrease in density of the BNKFT ceramics sintered at a higher temperature (1075 °C) may be due to the potassium and bismuth loss, and the presence of a porous microstructure

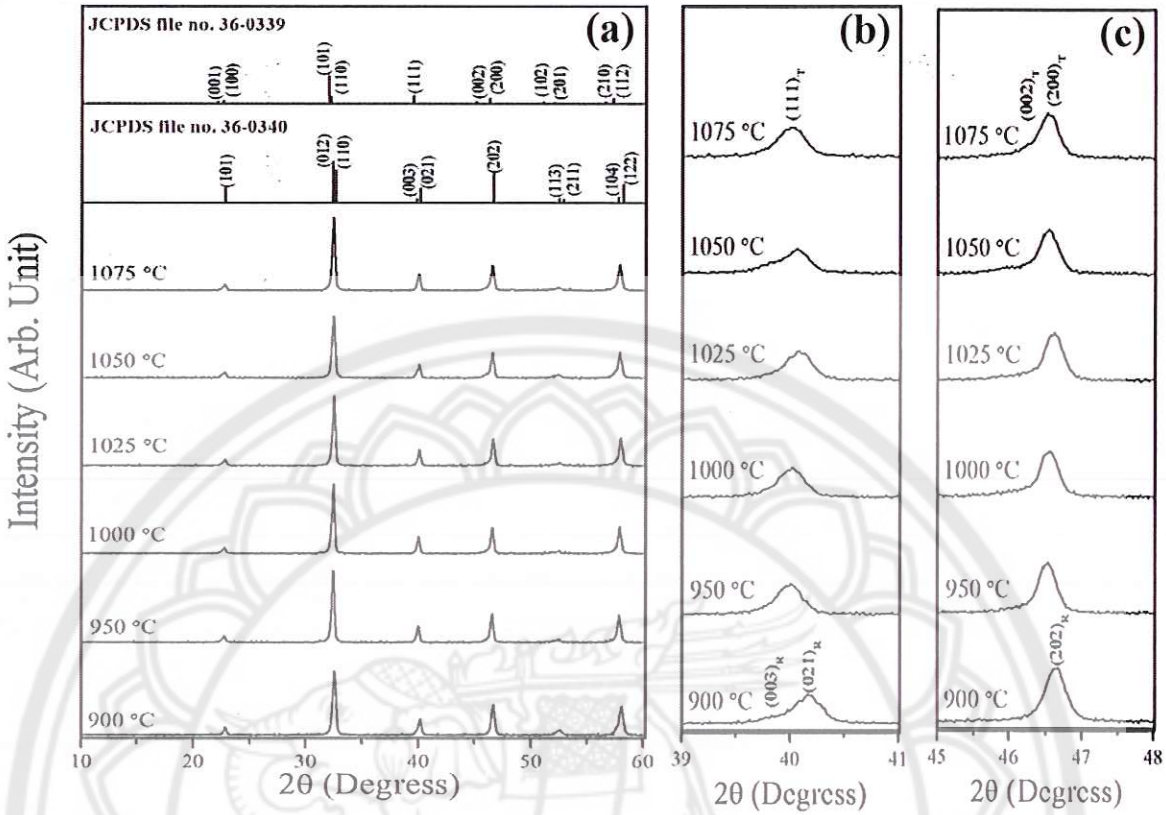

Fig. 4.7. X-ray diffraction patterns of BNKFT0.18/0.03 sintered ceramics at various temperatures in the 2θ range of (a) 10°-60°, (b) 39°-41° and (c) 45°-48°.

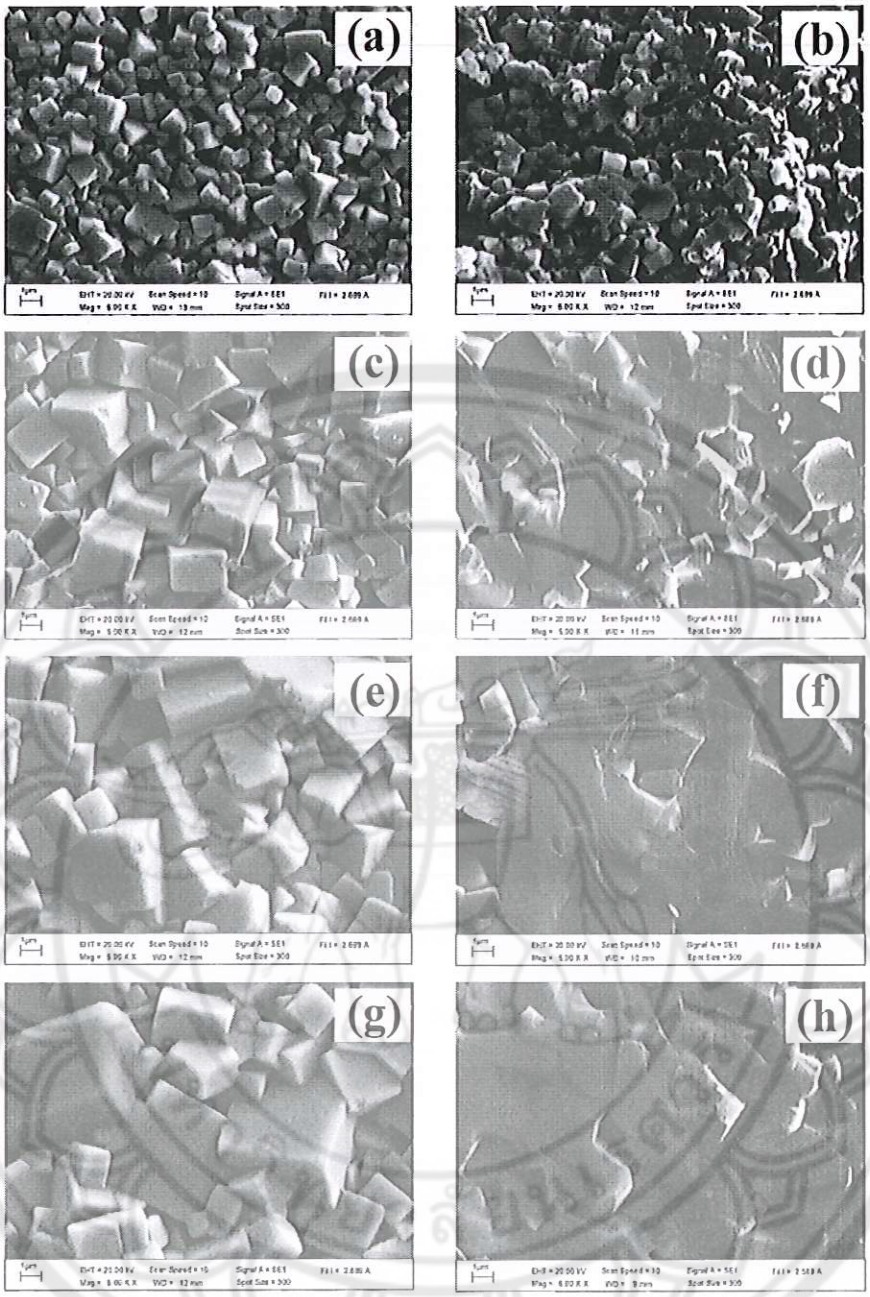

Fig. 4.8. Surface morphologies and cross-sectional micrographs of the BNKFT0.18/0.03 sintered ceramics at various temperatures: (a) and (b) sintered at 950 °C, (c) and (d) sintered at 1000 °C, (e) and (f) sintered at 1050 °C, (g) and (h) sintered at 1075 °C.

The optimum sintering temperature of all samples was found at 1050 °C for 2 h, and it was then that the amounts of x and y on the crystal structure and microstructure were examined. The XRD patterns of BNKFT-x/0.03 ceramics are shown in Fig. 4.9(a)-(c). All the

samples exhibit a pure perovsktite structure, indicating that K^+ was diffused into the lattice to form a solid solution. In general, the rhombohedral structure is characterized by (003)/(021) peaks spitting between 39° and 41° and a single peak of (202) between 45° to 48° whereas a pure tetragonal structure is characterized by a single peak of (111) between 39° and 41° and (002)/(200) peaks splitting between 45° to 48°. For x=0.12, the (003)/(021) peaks splitting occurs in the 2θ range of 39° to 40° (Fig. 4.9(b)) and the (202) peak is asymmetric in the range of 45° to 47° (Fig. 4.9(c)). When there was an increase of x content, the (003)/(021) peak begin to merge into a single (111) peak and the (202) peak started to split into two peaks of (002)/(200), which revealed that the crystalline structure has two phases between rhombohedral and tetragonal coexisting. Furthermore, the increasing of x content is affected by the increasing of the tetragonal and decreasing of the rhombohedral phase

The XRD patterns of BNKFT-0.18/y ceramics are shown in Fig. 4.10(a)-(c). The entire samples show the pure perovskite structure. For y=0, in the 2θ range of 39° to 41°, the (003)/(021) peaks splitting is slight (Fig. 4.10(b)). The peak splitting diminishes and begins to merge into a single (111) peak with increasing y content from 0 to 0.07. Moreover, in the 2θ range of 45° to 48° of y=0, the peak showed an asymmetric shape (Fig. 4.10(c)). When there was an increase of y content, the peak became more asymmetric and skewed to the left side. These results indicated that the ceramics reveal coexistence between tetragonal and rhombohedral phases. The structure results are in good agreement with previous work.

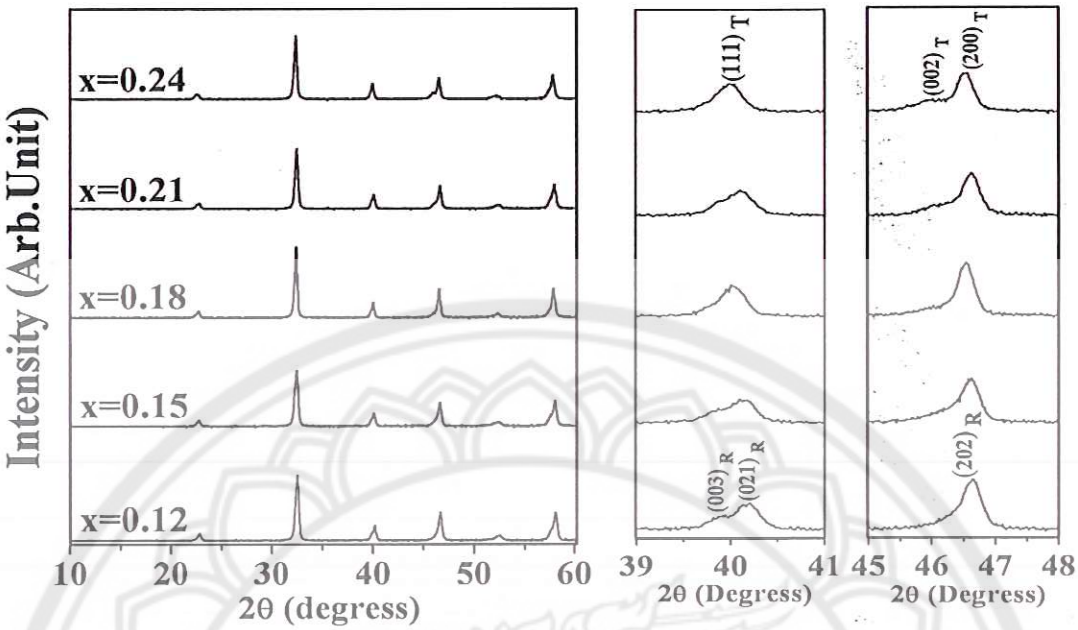

Fig. 4.9. X-ray diffraction patterns of BNKFT-*x*/0.03 sintered ceramics in the 2θ rang of (a) 10° to 60°, (b) 39° to 41° and (c) 45° to 48°.

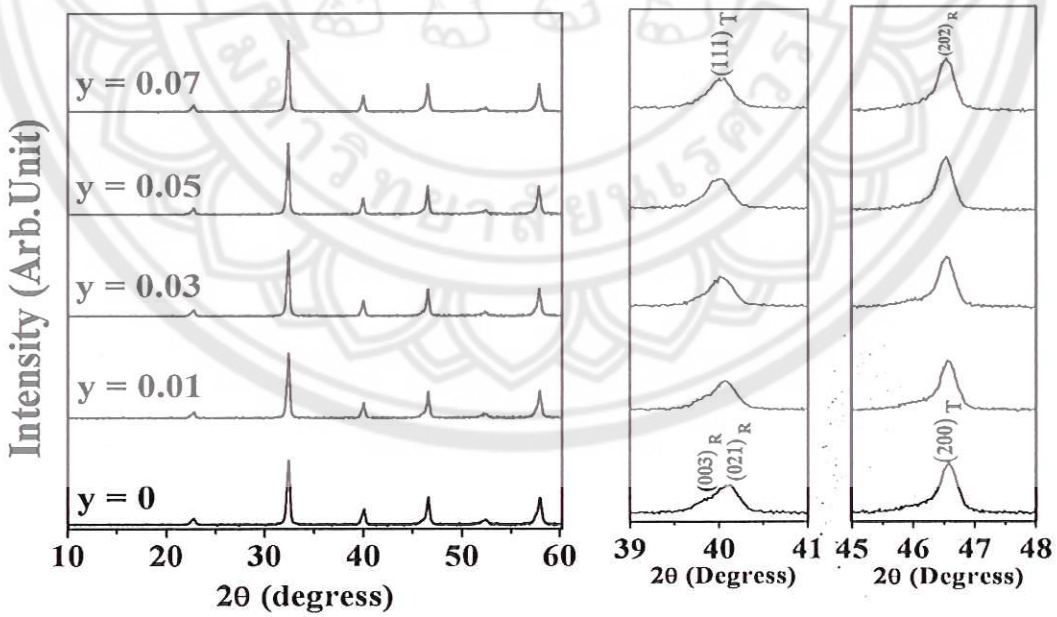

Fig. 4.10. X-ray diffraction patterns of BNKFT-0.18/*y* sintered ceramics.

The SEM micrographs of BNKFT-x/0.03 ceramics are shown in Fig. 4.11(a-c). All ceramics show a quasi-cubic morphology with clear grain boundaries. The average grain size decreases from 2.67 μm to 0.98 μm when the x content was increased from 0.12 to 0.24, as listed in Table 4.4. The grains become evidently smaller with increasing x content, which can be explained by the K^+ ion concentrates near grain boundaries and substantially reduced mobility as densification occurred. The decrease in the mobility of the grain boundary weakens the mass transport. As a result, grain growth is obviously inhibited and smaller grains are formed in the ceramic samples at a high concentration of x.

The SEM photomicrographs of BNKFT-0.18/y sintered pellets are shown in Fig. 4.11 (d)-(f). It can be seen that the grain exhibits an almost quasi-cubic morphology. The average grain size increased from 2.15 μm to 2.81 μm when increasing of y content (Table 4.4). The increased in grain size of the ceramics are due to the Fe^{3+} entering into the sixfold coordinated B-site to substitute for Ti^{4+} because of radius matching. The densities of BNKFT-0.18/y ceramics with different y content are listed in Table 4.4.

The measured density and relative density of the BNKFT-x/0.03 ceramics with different x content are listed in Table 4.3. The density increased and reached a maximum value of 5.85 g/cm^{-3} or ~ 96.6 % of the theoretical density obtained from the sample with x=0.18, and slightly decreased with x>0.18 (Table 4.3). The density increased from 5.57 g/cm^{-3} to 5.85 g/cm^{-3} (93.1% - 96.4% of theoretical density) when concentration of x increased from 0 to 0.03, and then dropped to 5.77 g/cm^{-3} (93.9% of theoretical one) with further increasing of y to 0.07.

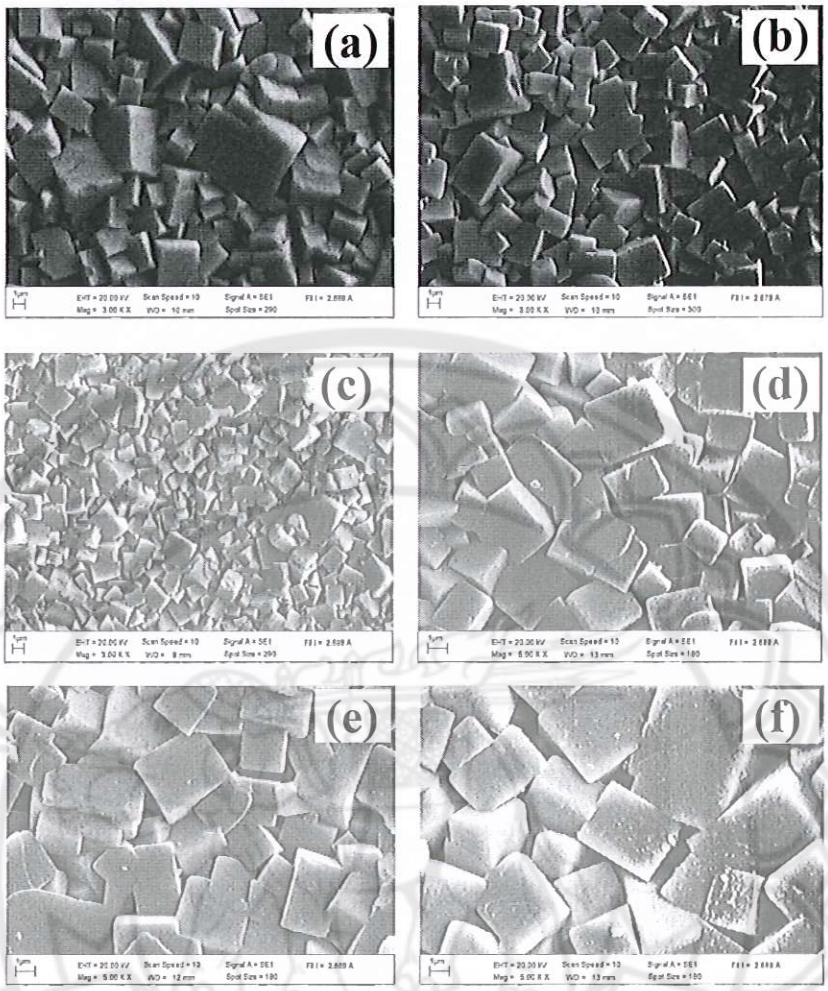

Fig. 4.11. SEM images of BNKFT-*x*/*y* sintered ceramics with (a) *x*= 0.12, (b) *x*=0.18, (c) *x*=0.21, (d) *y*=0, (e) *y*=0.03 and (f) *y*=0.07.

4.3 Effect of *x* and *y* on electrical properties of BNKFT Ceramics

4.3.1. Dielectric properties of BNKFT ceramics

Fig. 4.12(a) shows the temperature dependence of the dielectric constant (ε_r) of BNKFT-*x*/0.03 ceramics which were measured at 1 kHz. The dielectric constant showed two peaks (T_d at low temperature and T_c at high temperature) in all samples. The T_d is the temperature at which the phase transition from ferroelectric (rhombohedral) to anti-ferroelectric (tetragonal) occurred. T_c is the temperature at which the transition from tetragonal anti-ferroelectric (tetragonal) to cubic paraelectric (cubic) occurred. When there

was an increase of x, T_d of the sample shifted to the lower temperature from 185 °C to 94 °C whereas T_c shifts to higher temperature regions from 282° to 321 °C, as shown in Fig. 4.12(a). At Curie temperature, the maximum dielectric constant was observed in all samples. It tended to increase from 5,890 to 7,850 when the x content increased from 0.12 to 0.18. When further increasing x content to 0.24, ε_r decreased to 3,750, as listed in Table 4.4. The dielectric loss at T_c tended to decrease from 0.04 to 0.02 when the x content increased from 0.12 to 0.24, as shown in Table 4.4.

Temperature dependence of the dielectric constant (ε_r) of BNKFT-0.18/y ceramics which were measured at 1 kHz, as shown in Fig. 4.12(b). There are two abnormal temperature peaks which existed in all samples with different compositions. The T_d and T_c shifts to lower temperature regions from 131 °C to 123 °C and 294 °C to 282 °C with increasing y content from 0 to 0.07, as shown in Fig. 4.12(b). The result agrees with the result of Zhou *et al.* At T_c, the maximum dielectric constant tended to increase in value from 5,630 to 7,850 when the y content increased from 0 to 0.03. After that, the maximum dielectric constant of ceramics decreased as the concentration of y increased above 0.03, as listed in Table 4.4. The dielectric loss at T_c tended to increase from 0.02 to 0.04 when the y content increased from 0 to 0.07, as shown in Table 4.4. The ε_r and $\tan\delta$ at T_c (at 1 kHz) of all compositions is closely consistent with the result of previous work.

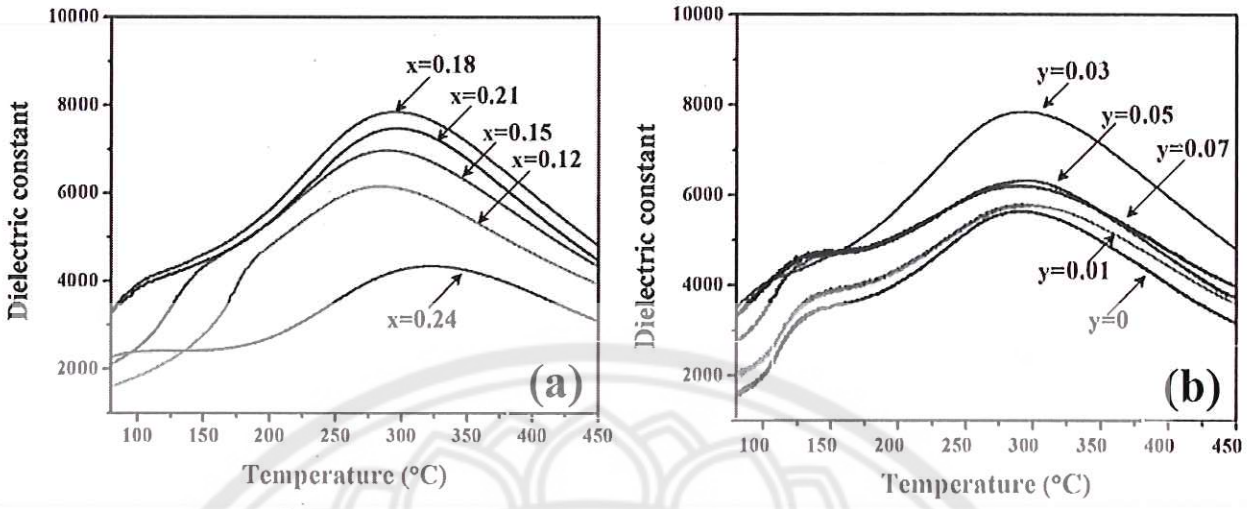

Fig. 4.12. The temperature dependences of dielectric constant (ε_r) of the (a) BNKFT-x/0.03 and (b) BNKFT-0.18/y ceramics.

4.3.2. Ferroelectric properties of BNKFT ceramics

The ferroelectric polarization–electric field (P-E) loop of BNKFT-x/0.03 ceramics measured at 40 kV/cm is shown in Fig. 4.13(a). All of composition, the P-E loops were not fully saturated. In literature of BKT (x) composition observation of saturated P-E behavior is reported to be difficult. The measured remnant polarization (P_r) of BNKFT-x/0.03 ceramics increased from 14.7 μC/cm^2 to the maximum value (18.6 μC/cm^2) at x=0.18, and then dropped to 4.4 μC/cm^2 with a further increase of x to 0.24. It is clear from P-E data that small additions of K^+ (up to x=0.18) improves the remnant polarization (P_r) values. The partial substitution of Na^+ (1.39 Å) ions by K^+ (1.64 Å) ions that have difference in ionic radii could cause distortion of unit cell, leading to the structure distortion of the oxygen octahedral and thus resulting in an increase of P_r. However, the decrease in P_r as x content increased (x>0.18) suggests that the high substitutions of K^+ ions for Na^+ ions would cause the decrease in relative displacement of unit cells. The ferroelectric polarization–electric field (P-E) loop of BNKFT-0.18/y ceramics is shown in Fig. 4.13(b). Typical rectangular loop can be observed for the BNKFT-0.18/0. With the y increased to 0.07, obviously pinched P-E loop

can be observed. At y=0, P_r and E_c is ~24.6 μC/cm^2 and ~22.4 kV/cm, respectively. With a further increase in y content to 0.07, P_r decrease to 7.6 μC/cm^2, as listed in Table 4.4.

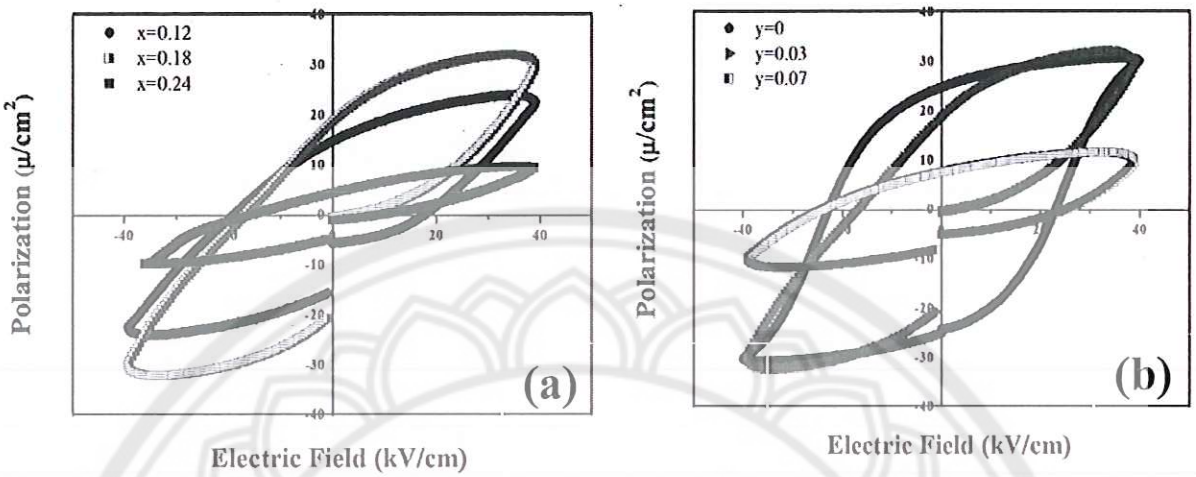

Fig. 4.13. Ferroelectric hysteresis loops of (a) BNKFT-x/0.03 and (b) BNKFT-0.18/y ceramics.

4.3.3 Piezoelectric properties of BNKFT ceramics

The piezoelectric coefficients of BNKFT-x/0.03 ceramics are illustrated in Fig. 4.14a. The piezoelectric coefficients d_{33} of all ceramics first increased and then decreased with increasing x content. The maximum d_{33} are obtained at x=0.18, which is 213 pC/N. The decrease of d_{33} due to the clamping effect association with oxygen vacancies hinders sufficient reorientation of ferroelectric domains during electrical poling. The d_{33} at x=0.18 showed a value higher than the result of previous work. The piezoelectric coefficient of BNKFT-0.18/y ceramics is shown in Fig. 4.14b. When y=0, the piezoelectric coefficients d_{33} are 164 pC/N. With increasing content of y, d_{33} reached the maximum values of 213 pC/N at y=0.03, and then dropped in value.

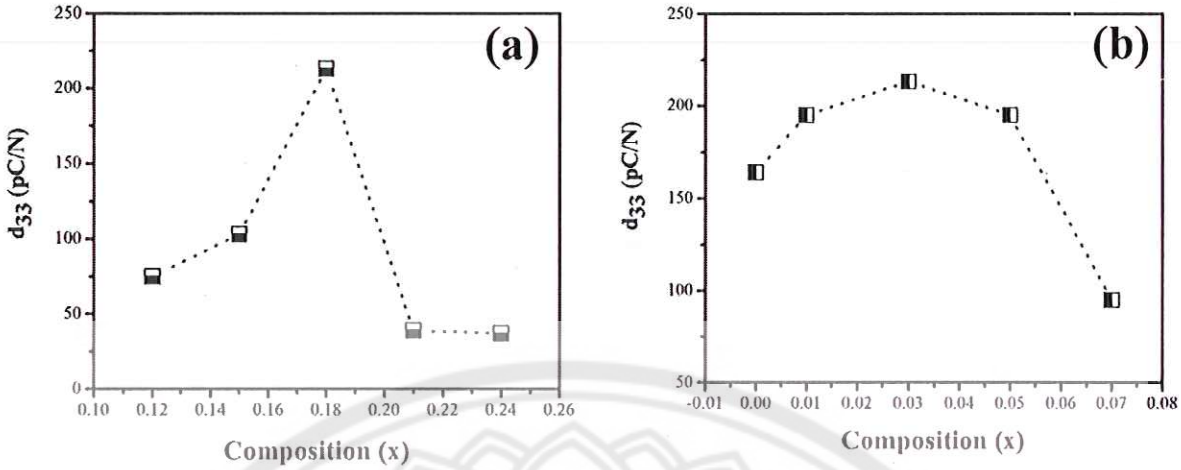

Fig. 4.14. Piezoelectric properties of (a) BNKFT-x/0.03 and (b) BNKFT-0.18/y ceramics.

Table 4.4. Average grain size, density, dielectric constant (ε_r), dielectric loss (tanδ), remnant polarizations (P_r) and coercive fields (E_c) of BNKFT-x/y ceramics

Composition	Average grain size (μm)	Measured density (g/cm^3)	Relative density (%)	ε_r at T_c	tanδ at T_c	P_r (μC/cm^2)	E_c (kV/cm)
x=0.12	2.67	5.73	94.6	5,890	0.04	14.7	19.0
x=0.15	2.41	5.79	95.7	6,970	0.03	18.0	23.8
x=0.18	2.39	5.85	96.6	7,850	0.02	18.6	16.3
x=0.21	1.33	5.79	94.1	7,310	0.02	24.2	24.2
x=0.24	0.98	5.57	92.1	3,750	0.02	4.4	15.2
y=0	2.15	5.57	93.1	5,630	0.02	24.6	22.4
y=0.01	2.23	5.63	93.8	5,640	0.02	19.6	21.9
y=0.03	2.44	5.85	96.4	7,850	0.02	18.6	16.9
y=0.05	2.73	5.80	95.1	6,330	0.03	17.2	24.4
y=0.07	2.81	5.77	93.9	6,320	0.04	7.6	24.7

CHAPTER 5
CONCLUSIONS

Lead free BNKFT ceramics were synthesized by the combustion technique. The optimal calcination and sintering conditions were found to be 750◦C for 2 h and 1050◦C for 2 h, respectively. The calcination and sintering temperatures directly affected the phase formation, microstructure, density and electrical properties. The lattice parameter of a increased with increasing x and y content. The SEM images indicated that with increasing x content, particle size decreases. But with increasing y content, the variation of the particle size is opposite. The highest density (ρ =5.85 g/cm3), superior dielectric properties at T_c (ε_r = 8,530 and tanδ = 0.02), remnant polarization measured at 40 kV/cm (20.1 μC/cm^2) and piezoelectric constant (d_{33} = 213pC/N) were obtained from the sample sintered at 1050◦C.

The variations of x and y contents directly affect the crystal structure, microstructure, density, dielectric, ferroelectric and piezoelectric properties of the BNKFT-x/0.03 and BNKFT-0.18/y ceramics. The XRD indicated that the ceramics possess pure single phase of perovskite structure, indicating that K^+ and Fe^+ have diffused into the lattice. With increasing x and y contents, grain size decreases and increases, respectively. The optimum electric properties can be obtained at x=0.18 and y=0.03, as follows: ρ=5.85 g/cm^3, ε_r=7850, tan δ=0.02, P_r=20.1 μC/cm^2 (measured at 40 kV/cm) and d_{33}=213 pC/N. With superior electric properties, this work indicates that the BNKFT-x/y ceramics prepared by the combustion technique are better than the BNKFT-x/y ceramics prepared by solid state.

REFERENCES

1. Z. Yang, B. Liu, L. Wei and Y. Hou, "Structure and electric properties of (1-x)$Bi_{0.5}Na_{0.5}TiO_3$ –x$Bi_{0.5}K_{0.5}TiO_3$ ceramics near morphotropic phase boundary" *Meter. Res. Bull.* **43** (2008) 81.
2. G.A. Smolenskii, V.A. Isupv, A.I. Agranovskaya and N.N. Krainik, "Some Properties of Bismuth Perovskites" *Sov. Phys. Solid state.* **2** (1961) 2584.
3. T. Takennaka, K. Maruyama and K. Sakata, "($Bi_{0.5}Na_{0.5}$)TiO_3-$BaTiO_3$ System for Lead-Free Piezoelectric Ceramics" *Jpn. J. Appl. Phys.* **30** (1991) 2236.
4. H. Nagata and T. Takenaka, "Lead-Free Piezoelectric Ceramics of ($Bi_{0.5}Na_{0.5}$)TiO_3–0.5(Bi_2O_3·Sc_2O_3) System" *Jpn. J. Appl. Phys.* **36** (1997) 6055.
5. H. Xinyou, G. Chunhua, C. Zhigang and L. Huiping, "Influence of Composition on Properties of BNT-BT Lead-F'ree Piezoceramics" *J. Rare Earths.* **24** (2006) 321.
6. Y. Li, W. Chen, J. Zhou, H. Sun and R. Xu, "Dielectric and piezoelecrtic properties of lead-free ($Na_{0.5}Bi_{0.5}$)TiO_3–$NaNbO_3$ ceramics" *Meter. Sci. Eng. B.* **112** (2004) 5.
7. Y. Watanable, Y. Hiruma, H. Nagata and T. Takenaka, "Phase transition temperatures and electrical properties of divalent ions (Ca^{2+} ,Sr^{2+} and Ba^{2+}) substituted ($Bi_{0.5}Na_{0.5}$)TiO_3 ceramics" *Ceram. Inter.* **34** (2008) 761.
8. C. Zhou, X. Liu,W. Li, C. Yuan, "Dielectric and piezoelectric properties of $Bi_{0.5}Na_{0.5}TiO_3$ –$Bi_{0.5}K_{0.5}TiO_3$ –$BiCrO_3$ lead-free piezoelectric ceramic" *J. Alloys. Compd.* **478** (2009) 381.
9. P. Fu, Z. Xu, R. Chu, W. Li, Q. Xie, G. Zang, "Effects of Eu_2O_3 on the structure and electrical properties of 0.82$Bi_{0.5}Na_{0.5}TiO_3$-0.18$Bi_{0.5}K_{0.5}TiO_3$ lead-free piezoelectric ceramics" *Curr. Appl. Phys.* **11** (2011) 822.

10. X.X.Wang, X.G. Tang and H.L.W. Chan, "Electromechanical and ferroelectric properties of $(Bi_{0.5}Na_{0.5})TiO_3$–$(Bi_{0.5}K_{0.5})TiO_3$–$BaTiO_3$ lead-free piezo-electric ceramics", *Appl. Phys. Lett.* **85** (2004) 91.

11. J. Shieh, K.C. Wu and C.S. Chen, "Switching characteristics of MPB compositions of $(Bi_{0.5}Na_{0.5})TiO_3$ –$BaTiO_3$ –$(Bi_{0.5}K_{0.5})TiO_3$ lead-free ferroelectric ceramics" *Acta Mater*. **55** (9) (2007) 3081.

12. Y. Hiruma, H. Nagata and T. Takenaka, "Phase transition temperatures and piezoelectric properties of $(Bi_{0.5}Na_{0.5})TiO_3$–$(Bi_{0.5}K_{0.5})TiO_3$ –$BaTiO_3$ lead-free piezoelectric ceramics", *Jpn. J. Appl. Phys*. **45** (2006) 7409.

13. C. Zhou, X. Liu, W. Li and C. Yuan, "Microstructure and electrical properties of $Bi_{0.5}Na_{0.5}TiO_3$ –$Bi_{0.5}K_{0.5}TiO_3$ – $LiNbO_3$ lead-free piezoelectric ceramics" *J. Phys. Chem. Solid*. **70** (2009) 541.

14. A. Singh and R. Chatterjee, "Structural, electrical, and strain properties of stoichiometric $1-x-yBi_{0.5}Na_{0.5}TiO_3-xBi_{0.5}K_{0.5}TiO_3-yNa_{0.5}K_{0.5}NbO_3$ solid solutions" *J. Apply Phys*. **109** (2011) 024105.

15. Z. Yang, Y. Hou, H. Pan and Y. Chang, "Structure, microstructure and electrical properties of $(1-x-y)Bi_{0.5}Na_{0.5}TiO_3$ –$xBi_{0.5}K_{0.5}TiO_3$ –$yBi_{0.5}Li_{0.5}TiO_3$ lead-free piezoelectric ceramics" *J. Alloys. Compd*. **480** (2009) 246.

16. D. Lin, Q. Zheng and C. Xu, "Structure, electrical properties and temperature characteristics of $Bi_{0.5}Na_{0.5}TiO_3$ –$Bi_{0.5}K_{0.5}TiO_3$–$Bi_{0.5}Li_{0.5}TiO_3$ lead-free piezoelectric ceramics" *Appl. Phys A*. **93** (2008) 549.

17. C.R. Zhou, X.Y. Liu, W.Z. Li and C.L. Yuan, "Dielectric relaxor behavior of $Bi_{0.5}Na_{0.5}TiO_3$ –$Bi_{0.5}K_{0.5}TiO_3$–$BiFeO_3$" *solid state communications* **149** (2009) 481.

18. Q. Zhou, C. Zhou, H. Yang, C. Yuan and W. Li, "Dielectric properties and depolarization temperature of $Bi_{0.5}Na_{0.5}TiO_3$ –$Bi_{0.5}K_{0.5}TiO_3$–$BiFeO_3$ lead-free ceramics" *Physica B* **405** (2010) 613.

19. C. Zhou, X. Liu, W. Li and C. Yuan, "Structure and piezoelectric properties of $Bi_{0.5}Na_{0.5}TiO_3$ –$Bi_{0.5}K_{0.5}TiO_3$–$BiFeO_3$ lead-free piezoelectric ceramics" *Mater. Chem. Phys.* **114** (2009) 832.

20. A Thongtha, K Angsukased and T Bongkarn, "Fabrication of $(Ba_{1-x}Sr_x)(Zr_xTi_{1-x})O_3$ ceramics prepared using the combustion technique" *Smart Mater. Struct.* **19** (2010) **7**.

21. P. Julphunthong and T. Bongkarn, "Phase formation, microstructure and dielectric properties of $Ba(Zr_{0.1}Ti_{0.9})O_3$ ceramics prepared via the combustion technique" *Curr. Appl. Phys.* Inpress.

22. U. Chaimongkon, A. Thongtha and T. Bongkarn, "The effects of firing temperatures and barium content on phase formation, microstructure and dielectric properties of lead barium titanate ceramics prepared via the combustion technique" *Curr. Appl. Phys.* Inpress.

23. A. Thongtha and T. Bongkarn, "Phase Formation and Microstructure of Barium Zirconate Ceramics Prepared Using the Combustion Technique" *ferroelectrics.* **383** (2009) 33.

24. R. Pampuch, "Advanced HT Ceramic Materials via Solid Combustion" *J. Euro. Ceram. Soc.* **19** (1999) 2395.

25. A.G. Merzhanov, "Combustion processes that synthesize meterials" *J. Meter.process. Technol.* **56** (1996) 222.

26. K.C. Patil, S.T. Aruna and T. Mimani, "Combustion synthesis: an update" *Curr. Opin. Solid State Mater. Sci.* **6** (2002) 507.

27. B.M. Wul and I.M. Goldman, "Dielectric constants of titanate of matals of the second grop" *Dokl. Akad. Nuak SSSR* **46** (1945) 154.

28. A.V. Hippel, R.G. Breckenridge, F.G. Chesley and L. Tisza, "High dielectric constant ceramics" *Ind. Eng. Chem. Res.* **38** (1946) 1097.

29. H. Haertling, "Ferroelectric Ceramics: History and Technology" *J. Am. Ceram. Soc.* **82** (1999) 797.

30. B. Jaffe, W.R. Cook, and H. Jaffe, Piezoelectric ceramics, India : Ceramic Book and Liturature Service, 1971.

31. A.J. Moulson and J.M. Herbert, Electroceramics. New York, Wiley- Interscience, 2003.

32. X. Yuhuan, Ferroelectric Materials and Their Applications, Natherland : Elsevier Science Publishers B.V., 1991.

33. J. Fousek, "Joseph Valasek and the Discovery of Ferroelectricity" *Proc. IEEE*, (1995) 1.

34. C. B. Sawyer and C. H. Tower, "Rochelle Salt as a Dielectric" *Phys. Rev.* **35** (1930) 269.

35. Y. M. Chiang, D. P. Birnie and W. D. Kingery, Physical Ceramics, New York, John Wiley & Sons, 1997.

36. B. Jaffe, W. R. Cook and H. Haffe, Piezoelectric Ceramics, New York, Academi Press, 1971.

37. F. Jona and G. Shirane, Ferroelectric Crystal, New York, Pergamon Press, 1962.

38. H. Megaw, Ferroelectricity in Crystals, Methuen, London, 1957.

39. K. Uchino, Piezoelectric Actuators and Ultrasonics Motors, Boston, Kluwer Academic Publishers, 1997.

40. G. A. Smolenskii, V. A. Isupov and A. I. Agranovskaya, "New Ferroelectrics of Complex Composition of the Type $A^{2+}(BI_{3+}\ BII_{5+})O_6$ I. " *Sov. Phys. Solid State*, **1** (1958) 150.

41. K. Uchino and S. Nomura, "Critical Exponent of the Dielectric Constants in Diffused-Phase-Transition Crystals" *Ferroelectrics Lett. Sect.* **44** (1982) 55.

42. C. A. Randall and A. S. Bhalla, "Nanostructure-Property Relations in Complex Lead Perovskites" *Jpn. J. Appl. Phys.* **29** (1990) 327.

43. C. Kittel, "Theory of Antiferroelectric Crystals" *Phys. Rev.* **82** (1951) 729.

44. Chiang, Y. Physical Ceramics, John Wiley & Sons, New York,1997

45. X.X. Wang, X.G. Tang, K.W. Kwok. H.L.W. Chan and C.L. Choy, "Effect of excess Bi_2O_3 in the electrical properties and microstructure of $(Bi_{0.5}Na_{0.5})TiO_3$ ceramics" *Appl. Phys. A* **80** (2005) 1071.

46. Y. Hiruma, H. Nagata and T. Takenaka, "Thermal depoling process and piezoelectric properties of bismuth sodium titanate ceramics" *J. Appl. Phys.* **105** (2009) 084112.

47. W.C. Lee, C.Y. Huang, L.K. Tsao and Y.C. Wu, "Chemical composition and tolerance factor at the morphotropic phase boundary in $(Bi_{0.5}Na_{0.5})TiO_3$-based piezoelectric ceramics" *J. Euro. Ceram. Soc.* **29** (2009) 1443.

48. M.M. Lencka, M. Oledzka and R.E. Riman, "Hydrothermal synthesis of sodium and potassium bismuth titanate" *Chem. Mater.* **12** (2000) 1323.

49. B.V. Bahuguna Saradhi, K. Srinivas, G. Prasad and S.V. Suryanarayana, "Impedance spectroscopic studies in ferroelectric $(Bi_{0.5}Na_{0.5})TiO_3$" *Mater. Sci. Eng B.* **98** (2003) 10.

50. R. Zuo, S. Su, Y. Wu J. Fu, M. Wang and L. Li, "Influence of A-site nonstoichiometry on sintering, microstructure and electrical properties of $(Bi_{0.5}Na_{0.5})TiO_3$ ceramics" *Mater. Chem. Phys.* **110** (2008) 311.

51. C. Xu, D. Lin, and K. W. Kwok, "Structure, electrical properties and depolarization temperature of $(Bi_{0.5}Na_{0.5})TiO_3$-$BaTiO_3$ lead-free piezoelectric ceramics" *Solid State Sci.* **10** (2008) 934.

52. G.A. Smolenskii, V.A. Isupov, A.I. Agranovskaya, N.N. Krainik, "New Ferroelectrics of Complex Composition." *Sov. Phys.-Solid State* **2** (1961) 265.

53. P. Vijaya Bhaskar RaO and T. Bhima Sankaram, "Impedance spectroscopy studies of $K_{0.5}Bi_{0.5}TiO_3$" *J. Electroceram* **25** (2010) 60.

54. V.V. Ivanova, A.G. Kapyshev, Y.N. Venevtsev and G.S. Zhdanov, "X-ray determination of the symmetry of elementary cells of the ferroelectric materials $(K_{0.5}Bi_{0.5})TiO_3$ and $(Na_{0.5}-Bi_{0.5})TiO_3$ and of high-temperature phase transitions in $(K_{0.5}Bi_{0.5})TiO_3$" *Izv. Akad. Nauk SSSR* **26** (1962) 798.

55. Y. Hou, M. Zhu, L. Hou, J. Liu, J. Tang, H. Wang and H. Yan, "Synthesis and characterization of lead-free $K_{0.5}Bi_{0.5}TiO_3$ ferroelectrics by sol-gel technique" *J. Crystal Growth* **273** (2005) 500.

56. Y. Hiruma, R. Aoyagi, H. Nagata and T. Takenaka, "Ferroelectric and piezoelectrics of $(K_{0.5}Bi_{0.5})TiO_3$ ceramics" *J. Appl. Phys.* **44** (2005) 5040.

57. J. Yang, Y. Hou, C. Wang, M. Zhu and H. Yan, "Relaxor behavior of $(K_{0.5}Bi_{0.5})TiO_3$ ceramics derived from molten salt synthesized single-crystalline nanowires" *Appl. Phys. Lett.* **91** (2007) 023118.

58. Y. Hiruma, K. Marumo, R. Aoyagi, H. Nagata and T. Takenaka, "Ferroelectric and piezoelectric properties of $(K_{0.5}Bi_{0.5})TiO_3$ ceramics fabricated by hot-pressing method" *J. Electriceram* **21** (2008) 296.

59. T. Takenaka, K. Maruyama and K. Sakata, "$(Bi_{0.5}Na_{0.5})TiO_3$-$BaTiO_3$ System for Lead-Free Piezoelectric Ceramics." *Jpn. J. Appl. Phys.* **1** (1991) 30 2236.

60. X. Wang, H.L.W. Chan and C.L. Choy "$(Bi_{0.5}Na_{0.5})TiO_3$ -$Ba(Cu_{0.5}W_{0.5})O_3$ Lead-free piezoelectric" *J. Am. Ceram. Soc.* **86** (2003) 1809.

61. A. Sasaki, T. Chiba, Y. Mamiya, E. Otsuki, "Dielectric and Piezoelectric Properties of $(Bi_{0.5}Na_{0.5})TiO_3$–$(Bi_{0.5}K_{0.5})TiO_3$ Systems" *Jpn. J. Appl. Phys.* **38** (1999) 5564.

62. T. Takenaka, H. Nagata and Y. Hiruma, "Phase Transition Temperatures and Piezoelectric Properties of $(Bi_{0.5}Na_{0.5})TiO_3$-and $(Bi_{0.5}K_{0.5})TiO_3$-Based Bismuth Perovskite Lead-Free Ferroelectric Ceramics" *IEEE Trans. Ultrason. Ferroelectr. Freq. Control* **56** (2009) 1595.

63. N. Yasuda and J. Konda, "Successive paraelectric-antiferroelectric-ferroelectric phase transitions in highly ordered perovskite lead ytterbium tantalate" *Appl. Phys Lett.* **62** (1995) 1995.

64. T. Takenaka and H. Nagata, "Current status and prospects of lead-free piezoelectric ceramics" *J. Eur. Ceram. Soc.* **25** (2005) 2693.

65. B. J. Chu, D. R. Chen, G. R. Li, and Q. R. Yin, "Electrical properties of $Na_{0.5}Bi_{0.5}TiO_3$-$BaTiO_3$ ceramics" *J. Eur. Ceram. Soc.* 22 (2002) 2115.

66. Y. Lin, S. Zhao, N. Cai, J. Wu, X. Zhou and C.W. Nan, "Effects of doping Eu_2O_3 in the phase transformation and piezoelectric properties of $(Bi_{0.5}Na_{0.5})TiO_3$-based ceramics" *Meter. Sci. Eng. B.* **99** (2003) 449.

67. A. Herabut and A. Safari, "Processing and electromechanical properties of $(Bi_{0.5}Na_{0.5})_{(1-1.5x)}LaxTiO_3$" J. *Am. Ceram. Soc.* **80** (1997) 2954.

68. T. Takenaka, H. Nagata "Lead-free piezoelectric ceramics of $(Bi_{0.5}Na_{0.5})TiO_3$ $0.5(Bi_2O_3 \cdot Sc_2O_3)$ system" *Jpn. J. Appl. Phys.* **36** (1997) 6055.

69. C. Zhou and X. Liu, "Dielectric and piezoelectric properties of bismuth-containing complex perovskite solid solution of $Bi_{0.5}Na_{0.5}TiO_3$–$Bi(Mg_{0.7}Nb_{0.3})O_3$" *J. Mater. Sci.* **43** (20081) 1016.

70. C. Zhou and X. Liu, "Dielectric and piezoelectric properties of $Bi_{0.5}Na_{0.5}TiO_3$–$BaNb_2O_6$ lead-free piezoelectric ceramics" J. *Mater. Sci. Mater. Electron.* **19** (2008) 29.

71. K. Sakata, T. Takenaka and Y. Naitou, "Phase relations, dielectric and piezoelectric properties of ceramics in the system $(Bi_{0.5}Na_{0.5})TiO_3$–$PbTiO_3$" *Ferroelectrics* **131** (1992) 219.

72. M. Zou, H. Fan, L. Chen and W. Yang, "Microstructure and electrical properties of $(1-x)[0.82Bi_{0.5}Na_{0.5}TiO_3$-$0.18Bi_{0.5}K_{0.5}TiO_3]$-$xBiFeO_3$ lead-free piezoelectric ceramic" *J. Alloys. Compd.* **10** (2010) 1.

73. A. Hussain, C.W. Ahn, A. Ullah and J. S. Lee, I. W. Kim, "Dielectric, ferroelectric and field-induced strain behavior of $K_{0.5}Na_{0.5}NbO_3$-modified $Bi_{0.5}(Na_{0.78}K_{0.22})_{0.5}TiO_3$ lead-free ceramics" *Ceram. Inter.* **12** (2010) 00090.

74. A. Singh and R. Chatterjee, "Structure, electrical, and strain properties of stoichiometric $1-x-y(Bi_{0.5}Na_{0.5})TiO_3 - x(Bi_{0.5}K_{0.5}TiO_3)-y(Na_{0.5}K_{0.5})NbO_3$ " *J. Apply. Phys.* **109** (2011) 024105.

75. D. Lin, Q. Zheng, C. Xu and K.W. Kwok, "Structure, electrical properties and temperature characteristics of $Bi_{0.5}Na_{0.5}TiO_3$ –$Bi_{0.5}K_{0.5}TiO_3$ –$Bi_{0.5}Li_{0.5}TiO_3$ lead-free piezoelectric ceramics" *Appl. Phys. A.* **93** (2008) 549.

76. Y. Hiruma, H. Nagata and T. Takenaka, "Depolarization temperature and piezoelectric properties of $(Bi_{0.5}Na_{0.5})TiO_3$ –$(Bi_{0.5}Li_{0.5})TiO_3$ –$(Bi_{0.5}K_{0.5})TiO_3$ lead-free piezoelectric ceramics" *Ceram. Inter.* **35** (2009) 117.

77. S. L. Swartz and T. R. Shrout, "Fabrication of Perovskite Lead Magnesium Niobate", *Mater. Res. Bull.* **17** (1982) 1245.

78. W. E. Lee and W. M. Rainforth, Ceramic Microstructures Property Control by Processing, London, Chapman & Hall, 1994.

79. P. E. J. Flewitt and R.K. Wild, Microstructure Characterization of Materials and Alloys, London, I.O. Metals, 1985.